UTRECHT UNIVERSITY
Graduate School of Natural Sciences
Institute for Marine and Atmospheric research
and the
INSTITUT PIERRE-SIMON LAPLACE - Laboratoire
des Sciences du Climat et de l'Environnement

MASTER'S THESIS

Simulating the South American Monsoon System during the Mid-Miocene Climatic Optimum

presented by
Marius Alexander Schulz

06. November 2023

Dr. Pierre Sepulchre	**Supervisor**
Dr. Michiel Baatsen	**First Examiner**
Dr. Anna von der Heydt	**Second Examiner**

A thesis submitted in partial fulfillment of the requirements for the degree of Master of Science in Climate Physics

Abstract

Utilizing the Earth System Model IPSL-CM5A2 and the Atmosphere-Land Surface Model LMDZOR6_v2.2, I conduct simulations of the South American Monsoon System (SAMS) during the Mid-Miocene Climatic Optimum (MMCO), a warm period ∼15 Ma before present. A 3000-year IPSL-CM5A2 simulation is performed with Mid-Miocene boundary conditions, including a pCO_2 of 840 ppm, finding a MAT increase of 8.85 K compared to the preindustrial. Simulated MMCO SSTs are then used to force LMDZOR6 to benefit from a higher spatial resolution, more developed parameterizations of convection, and new radiative and soil hydrology schemes. For the positive SAMS phase in the MMCO, the simulations consistently demonstrate an intensification of the hydrological cycle in the core regions and decreased precipitation in the Central Andes and La Plata Basin, accompanied by a strengthening of all SAMS components apart from the South American Low-Level Jet. The main convective activity shifts from the SACZ to the eastern Amazon, resulting in a more northern Bolivian High, while the main SACZ activity relocates over the southern tropical Atlantic. Diverging signals are found for the MMCO's negative SAMS phase, with increasing precipitation in IPSL-CM5A2 and decreasing precipitation in LMDZOR6. Dynamical vegetation experiments show an expansion of tropical biomes up to 30°S. Dynamical versus static hydrological vegetation feedbacks are identified but found to be small compared to differences between model generations. The study shows how MMCO-warmth and paleogeography affect different parts of the monsoon circulation and might help to understand past, as well as possible future changes in the SAMS.

Contents

List of Figures

List of Tables

Acronyms and Abbreviations

AB Amazon Basin
AMOC Atlantic Meridional Overturning Circulation
BH Bolivian High
BP Brazilian Plateau
CA Central Andes
CAPE Convective Available Potential Energy
CAS Central American Seaway
CDS Copernicus Climate Data Store
CL Chaco Low
CPL Fully coupled mode
CRF Cloud radiative forcing
CV Constant vegetation
DJF December, January and February
DV Dynamic vegetation
EMIC Earth System Model of intermediate complexity
ENSO El Niño Southern Oscillation
ESM Earth System Model
GHG Greenhouse gases
GMAT Global Mean Annual Temperature
ITCZ Intertropical Convergence Zone
JJA June, July and August
LPB La Plata Basin
MAM March, April and May
MAT Mean Annual Temperature
MCS Mesoscale Convective Systems
MioMIP Miocene Model Intercomparison Project
MMCO Mid-Miocene Climatic Optimum
MMCT Mid-Miocene Climate Transition
NA Northern Andes
NESA North East South America
OLR Outgoing longwave radiation
P-E Precipitation minus evapotranspiration
PI Preindustrial
PFT Plant functional type
SACZ South Atlantic Convergence Zone
SALLJ South American Low-Level Jet
SAMS South American Monsoon System
SESA South East South America
SICZ South Indian Convergence Zone
SON September, October and November
SPCZ South Pacific Convergence Zone
SSA Southern South America
SST Sea Surface Temperature

1 Introduction

The South American Monsoon System (SAMS) is the most important climatic feature of South America (De Carvalho and Cavalcanti 2016). Its circulation induces significant seasonal changes in the hydrological cycle and has tremendous environmental and societal impacts (Marengo et al. 2012). The SAMS region contains the Amazon rain forest, an essential component of the climate system and suspected tipping point under deforestation and global warming (Nobre and Borma 2009). For these reasons, it is crucial to understand how the SAMS manifests in warmer climates. Paleoclimates, such as the Pliocene, are attractive simulation targets because they constitute an actual realization of a warmer climate at similar topographic boundary conditions. In recent years, the Miocene (23-5.33 Ma before present) has become a period of increasing interest, partially because the Pliocenes $p\mathrm{CO}_2$, which often serves as future analog, will soon be surpassed. The Mid-Miocene Climatic Optimum (MMCO) stands out as opposing the general Cenozoic cooling trend, and the most recent analog with global temperature more than 7 K higher compared to the preindustrial and $p\mathrm{CO}_2$ values as high as 800 ppm (Steinthorsdottir et al. 2021a). The MMCO is of further interest in paleoclimatology regarding how this strong warming can be explained. Past simulation studies had difficulties in reproducing Mid-Miocene warmth (Burls et al. 2021; Goldner et al. 2014), and different mechanisms like the paleoclimatic boundary conditions and unaccounted feedbacks have been theorized to explain this discrepancy (Henrot et al. 2017). Thus, it acts as a relatively recent analog to even further paleoclimates as the Eocene. The Miocene Model Intercomparison Project (MioMIP) has initiated an effort to standardize experiments and join resources to investigate this and other issues in reconstructing Miocene climate (Burls et al. 2021). This study adopts MioMIPs standards to simulate the MMCO's SAMS in order to contribute to the modeling efforts and to benefit from the comparability to existing simulations. My main interests are the properties of the seasonal South American circulation and hydrology in simulations of the MMCO, and how they compare to the modern SAMS. Further, I want to understand the dynamics of the observed climate and compare it to existing knowledge about the past South American climate, and understand how it is affected by different changing factors like the changes in thermodynamics, large scale dynamics, orography, sea surface temperature and vegetation cover.

To do so, I perform an equilibrium simulation of the MMCO using the Earth System Model (ESM) IPSL-CM5A2. To get an even better understanding of the SAMS and be able to improve upon known biases, I use the more accurate but less efficient next model version IPSL-CM6-LR to simulate the atmosphere-vegetation system using the equilibrated SSTs. Further, two dynamical vegetation simulations and two control simulations are performed to investigate the adapted vegetation cover and possible influences on the modeled SAMS. Chapter 2 contains a theoretical framework of the SAMS and a literature assessment on the MMCO and is followed by a method section (Ch. 3) containing the presentation of the used models and boundary conditions, as well as the simulation strategy, and summary of used analyses and data. In chapter 4, I assess the modern biases of the used ESMs relevant for simulating the South American climate before analyzing the equilibrium simulation of the MMCO in terms of assessing the global climate, the reproduced SAMS features and the regional hydrology (Chapter 5). Further, I assess the robustness of the simulation by

comparing it to IPSL-CM6-LR and assessing the mechanisms responsible for the difference in simulated climate and differences in the simulated vegetation cover before validating them using paleobotanical proxies. The report closes with a discussion on the mechanisms leading to the observed changes and the robustness of the presented estimate in the light of the known bias, existing MMCO simulations and proxies, as well as a critical reflection and outlook (cf. Ch. 6), followed by the conclusion (cf. Ch. 7).

2 Theory

2.1 The Modern South American Monsoon

Monsoons are seasonal climatic phenomena found in tropical and subtropical regions that cause a rainy summer season and a dry winter season (Geen et al. 2020). The reason for the seasonal hydrological change in monsoon systems is a reversal of wind, leading to moisture import from the ocean or prevailing dry, continental winds (ibid.). Historically, this reversal has been explained by the regional changes in the sea-breeze due to seasonal differences in thermal heating of land and ocean and denoted the seasonal climate in the indo-pacific region (Halley 1686; Gadgil 2018). While this paradigm has long been challenged on theoretical and observational grounds (Simpson 1921; Kothawale and Kumar 2002), it has only changed in recent decades following conclusive evidence against this hypothesis (Gadgil 2018). The modern theory views monsoons as phenomena caused by the global migration of the Hadley cell due to seasonally changing solar insolation (Geen et al. 2020). The subsequent shift of the Intertropical Convergence Zone (ITCZ) and (sub)-tropical winds leads to the formation of seasonal convergence zones such as the South Pacific Convergence Zone (SPCZ), the South Indian Convergence Zone (SICZ) and the South Atlantic Convergence Zone (SACZ), which cause distinct seasonal precipitation patterns in the respective regions (Geen et al. 2020; Espinoza et al. 2020). Unlike in other monsoon regions, northern South America shows year-round easterlies at lower levels. Because of this, the South American Monsoon System was not recognized as such until the late twentieth century, when the understanding and definition of the Monsoon regions changed (De Carvalho and Cavalcanti 2016).

2.1.1 Circulation

The South American monsoon is a climate phenomenon that occurs between approximately 5°N and 30°S, and alternates between a warm phase that sets on locally between September and November and lasts until April to May (Vera et al. 2006a). It brings large amounts of precipitation to the Amazon, Altiplano, La Plata Basin and the Brazilian Plateau. Its cold phase corresponds to the warm phase of the North American Monsoon during June through August, which peaks over Mexico but extends into northern South America, leading to a seasonal precipitation maximum on the Caribbean Coast and in the Northern Amazon (ibid.). Espinoza et al. (2020) analyze the modern seasonal hydrology thoroughly and find that the primary mechanism of this monsoon is the migration of the low-level easterlies, which transport moisture from the warm tropical Atlantic, and the subsequent movement of the subtropical westerlies. During austral winter, the easterlies are strongest in the Caribbean and can pass South America north of the Andes (north of 10°N) and over the lower Andes north of the equator. Upper-level westerlies dominate the continental flow south of 15°S and are strongest in the subtropical jet at about 30°S and 200 hPa. During austral summer, the easterlies and the entire Hadley cell migrate southward, weakening the westerlies and pushing them to 60°S−25°S with the jet migrating to 50°S. The low-level easterlies, moving to the southern hemisphere, are blocked by the Andean Cordillera, which extends well above the 600 hPa level throughout the tropics and subtropics of the Southern Hemisphere (ibid.). This creates a new circulation pattern that

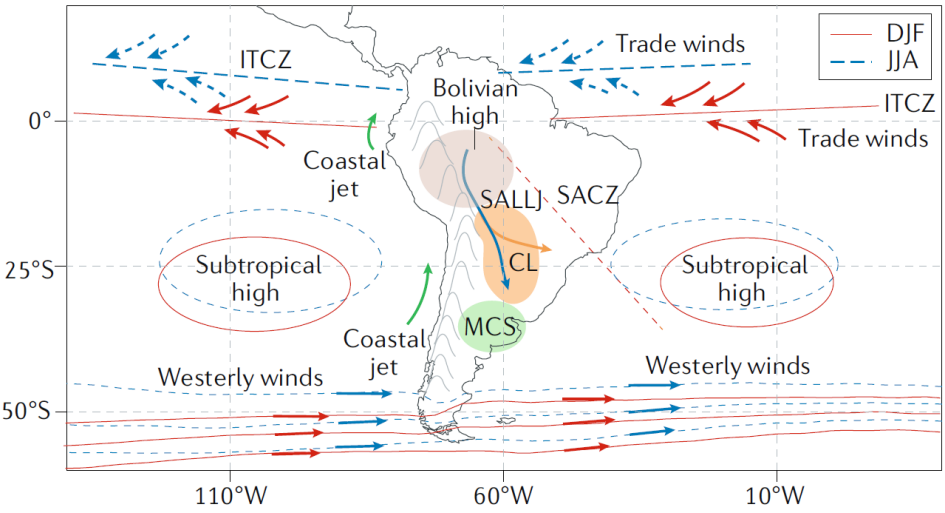

Figure 1: Schematic of the main components position of the SAMS circulation during JJA and DJF. MCS denotes the mesoconvective systems in South America in response to the moisture transport by the SALLJ (Cai et al. 2020).

forces the continental easterlies to turn south. The most prominent feature of this circulation is the South American Low-Level Jet (SALLJ), which manifests daily at 850 hPa east of the Andes, in two seasonally changing regimes (Liebmann and Mechoso 2011). It is most pronounced above 20°S in the warm season, when it blows from Amazonia along the tropical eastern slopes of the Andean, but persists in the cold season as an easterly jet on the Brazilian Plateau before turning southward at the slopes of the Altiplano (Marengo et al. 2004; Liebmann et al. 2004). The SALLJ is essential for the moisture transport from the Amazon to the La Plata basin (Marengo et al. 2004; Garreaud et al. 2009; Segura et al. 2020). Further, the SALLJ leads to a negative southward vorticity transport and thus contributes to the lower-level Sverdrup vorticity balance (Rodwell and Hoskins 2001). A pivotal feature of the warm SAMS mode is the Bolivian high (BH), an upper-tropospheric anticyclone in the Altiplano region (cf. Fig. 1). The BH is a Rossby wave response to the heavy convective precipitation in the Amazon, SACZ, and central Andes (Figueroa et al. 1995; Lenters and Cook 1997). Over the Amazon and southern Brazil to the South Atlantic, the convergence of moist trade winds forms the north-westerly oriented South Atlantic Convergence Zone (SACZ, cf. Fig. 2), which leads to heavy convection and precipitation (Van Der Wiel et al. 2015; Espinoza et al. 2020). The SACZ arises in short-lived multi-day events caused by the refraction of circular westerly vorticity wave trains at the BH (Figueroa et al. 1995), leading to a shear and equator-ward transport of the Rossby-waves (Van Der Wiel et al. 2015), inducing the north-west oriented cloudy band of intense convection and precipitation (ibid.). Although the SACZ is anchored in the ITCZ in the north-east, it is a distinct convective phenomenon (ibid.) that facilitates substantial precipitation over subtropical South America during the warm phase of the SAMS. Further features of the SAMS include the Chaco Low (CL) in south-eastern South America, which is a dynamic response to the Bolivian High and Subtropical Atlantic High and enhances the northwesterly moisture advation (cf. Fig.1) (Cai et al. 2020).

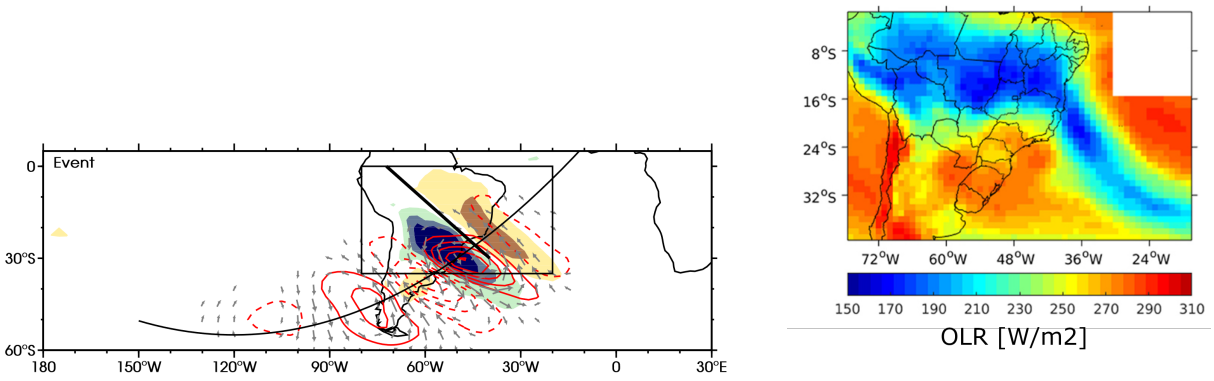

Figure 2: Left: Schematic of idealized SACZ event, showing OLR (shading), the 200 hPa vorticity anomaly and the wave track (Van Der Wiel et al. 2015). Right: OLR in W/m^2 (cloudiness proxy) during the SACZ episode of the 12-18th of January 2007, showing the position and intensity of the continental and Atlantic parts of the SACZ through (Rosa et al. 2020).

2.1.2 Hydrology

The onset of the rainy season begins in the central Amazon around late September and spreads to southeastern Brazil around late November (cf. Vera et al. 2006a, Fig. 2). At the same time, precipitation decreases in northern South America (Guyana Shield, Orinoco Basin and Llanos) (Espinoza et al. 2020). The source of the moisture is the easterlies that transport moisture from the warm Atlantic to the continent. The dynamics discussed in section 2.1.1 result in a southward transport and distribution of this moisture while interacting with the land cover and orography (ibid.). The Andean foothills order the flow and create regions of high precipitation as moist air rises at the mountains slopes (ibid.). Modeling experiments removing the Andes demonstrate the importance of the mechanical forcing of the Andes for the moisture transport to the central Andes and La Plata basin (Junquas et al. 2016). Studies by Zemp et al. (2014) and Staal et al. (2018) show that the moisture initially carried by the easterlies would be depleted after crossing the Amazon Basin if it was not for the Amazon rainforest, storing precipitated water and releasing it delayed through evapotranspiration. Through this cycle called *precipitation recycling*, the South American vegetation contributes significantly to the dispersion of moisture to the Andes and the southern regions of South America.
The dynamics of the SAMS is modulated by the El Niño Southern Oscillation (ENSO). During a positive ENSO phase, precipitation increases along the Ecuadorian and North Peruvian coasts, over the Altiplano and the La Plata Basin, and decreases in northern South America, the northern and central Amazon and the Brazilian Plateau (Córdova et al. 2022). During La Niña, northeast South America is anomalously wet, while the Brazilian Plateau is drier than in neutral phase. Cai et al. (2020) identify local forcings, such as elevated SSTs along the coast of Ecuador, and two atmospheric teleconnection pathways responsible for this effect. Elevated Pacific sea surface temperatures favor ascending motion in the west, altering the Walker circulation, leading to descending motion over central and east tropical SA, suppressing precipitation and resulting in a dry bias. The second teleconnection occurs through displacements of the quasi-stationary Rossby waves, which favor northwesterly advection of moisture to southeast South America (Silva

and Ambrizzi 2006).

2.2 The Climate of the Mid-Miocene Climatic Optimum

The Miocene epoch lasted from 23.03 Ma to 5.33 Ma before the present. Together with the preceding Oligocene, it belongs to the "coolhouse" climate of the Cenozoic, following the even warmer Paleocene and Eocene (Westerhold et al. 2020). The Miocene is the youngest epoch with marked tectonic changes towards modern topography, aside from morphological processes related to glaciation (Potter and Szatmari 2009). The Oligocene-Miocene transition is characterized by an increase in δ^{18}O associated with an expansion of the Antarctic ice sheet (Steinthorsdottir et al. 2021a). During most of the early Miocene (Burdigalian), the δ^{18}O is mainly forced by orbital cycles (ibid.). The MMCO (16.75-14.5 Ma) began in the early Burdigalian and is characterized by a drop in δ^{18}O (Steinthorsdottir et al. 2021b), marking decreasing ice sheet volume and increasing bottom water Temperatures (Frigola et al. 2018), and lasted until the middle Langhian, where δ^{18}O increased again, initiating the Mid-Miocene Climate Transition (MMCT) (cf. Fig. 2.2). Goldner et al. (2014) estimate the GMAT at 7.6 ± 2.3°C compared to the preindustrial from available ocean proxies, which compares well to other estimates (Steinthorsdottir et al. 2021a). The CO_2 concentration during the MMCO can be estimated from both geochemical and biological proxies. First, the δ^{11} boron isotope fraction in marine carbonates can give an estimate of ocean pH and thus of carbonate and CO_2 levels. Secondly, the δ^{13}C fractionation in alkenones produced by fossil algae can give an estimate of CO_2 levels when temperature proxies are available (Rae et al. 2021). During most of the Miocene, the CO_2 concentration ranged between 300 to 600 ppm (Burls et al. 2021). During the MMCO, independent proxies suggest levels of ∼450-550 ppm (Steinthorsdottir et al. 2021a). Some reconstructions show peaks higher than 800 ppm (Stoll et al. 2019; Sosdian et al. 2018), which is required by most models to reproduce mid-Miocene warmth (Burls et al. 2021). /textwidth/textwidth

2.2.1 Bathymetry and Topography

The continental configuration during the MMCO resembled the modern continental configuration, but there were significant differences regarding ocean gateways. The Central American Seaway (CAS) remained open until the late Miocene or early Pliocene, allowing for low-latitude exchange between the Pacific and the Atlantic Ocean (Groeneveld et al. 2014). The Bering-Strait and the Canadian Archipelago were closed, isolating the Arctic Ocean from the North Pacific and the Labrador Sea (Burls et al. 2021). Where there is now the Mediterranean Sea and the Arabian Peninsula, the remainder of the Tethys Sea connected the Atlantic Ocean with the Indian Ocean (ibid.). At the same time, a strait called the Indonesian Gateway at the modern Banda Sea allowed for deep water exchange between the east Indian Ocean and the West Pacific (Kuhnt et al. 2004). A detailed reconstruction of the tectonic configuration at 15 Ma is displayed in section 3, Figure 4.
This early and mid-Miocene was an orogenic active period contributing to the genesis of the Himalayas, Andes, and Alps, which was finished by the late Miocene (Steinthorsdottir et al. 2021a). Tectonic reconstructions exhibit a north-westward shift of the South American Continent by approximately two degrees respectively (cf. Burls et al. 2021).

The evolving bathymetry influenced the oceanic circulation patterns. Modeling studies suggest that reconstructed circulations with deep-water formation both in the North Atlantic and North Pacific are caused by the low-latitude connections of the Ocean-Basins (Von Der Heydt and Dijkstra 2008).

2.2.2 Ice Sheets

The ice sheet volume can be estimated using $\delta^{18}O$ deep sea records for the Cenozoic, but are relatively uncertain for the mid-Miocene (Oerlemans 2004). The early Miocene exhibits a significant Antarctic ice sheet expansion (Liebrand et al. 2017), which declined to a minimum during the MMCO (De Vleeschouwer et al. 2017). An Antarctic ice sheet was located in the Wilkes Basin in east Antarctica throughout the MMCO (Sangiorgi et al. 2018), which is estimated to have amounted to 25-70% of the present East Antarctic ice sheet (Pekar and DeConto 2006). Gasson et al. (2016) performed several dynamic ice sheet simulations during the mid-Miocene and estimated the ice sheet volume at 11.5 km^3 for 3xPI CO_2 forcing. Other parts are shown to have been covered by boreal vegetation (Lewis et al. 2008). The relatively little glaciation in the MMCO was followed by a rapid expansion of the Antarctic ice sheet consistent with linear cooling (Langebroek et al. 2009). The existence of an ice sheet in Greenland is unresolved (Steinthorsdottir et al. 2021b). There is limited evidence for sea-terminating glaciers throughout the Miocene, but proxies indicating perennial ice sheets and large-scale glaciation are concentrated in the cooler late Miocene (ibid.).

2.2.3 Vegetation

The vegetation during the MMCO differed significantly from the preindustrial vegetation, which is due mainly to different climatic conditions and different species composition. The paleorecord shows that biomes were situated at higher latitudes than their modern counterparts, sustained by generally elevated temperature and humidity levels. In the Langhian, proxies are pointing to temperate forests extending above 60°N (Pound et al. 2012; Henrot et al. 2017). Antarctic pollen records are evidence of the presence of woody vegetation, pointing to the existence of a tundra until after the MMCO (Anderson et al. 2011). Tropical rainforests seem to have expanded but were confined to the Tropics of Capricorn and Cancer, even if temperatures at higher latitudes seemed suitable (Jaramillo and Cárdenas 2013). A tropical wetland system called *Pebas* covered large parts of the East Amazon Basin, which consisted of connected lakes, swamps, and forested floodplains (Jaramillo 2023). Across the Neogene, tropical forests shrank while grasslands and deserts spread, connected to a general cooling and drying of the climate (Steinthorsdottir et al. 2021b). For the Langhian, there is evidence of an early Atacama desert and C3-dominated temperate grasslands in southern South America (Pound et al. 2012). C4 grasses, which are better adapted to hydrological stress, are not documented to have abundantly occurred until ∼10 Ma (Jaramillo 2023; Steinthorsdottir et al. 2021a).

2.2.4 Precipitation and Monsoons

The existence of monsoons can be traced back to the Paleogene (Spicer 2017). this is supported by several pathways of evidence to reconstruct past precipitation and their variability, giving an insight into the amount and seasonality of precipitation. For example, mammal tooth enamel can be used to trace the aridification of southern South America at the onset of the MMCO (Trayler et al. 2020) and can give sub-annual resolution. Likewise, Scholz et al. (2020) investigated mollusk growth to find a high seasonality of precipitation in the Caribbean during the MMCO, suggesting the presence of a monsoon system. A common method to reconstruct past hydrologies from proxies is the so-called *co-existence approach*. Using modern relatives of plants for which life-supporting climatic conditions are known, multiple coexisting species can be used to constrain the possible corridor of paleo-climatic parameters (cf. Bruch et al. 2011). This approach shows reduced seasonality of precipitation in Europe during the mid-Miocene. Studies on paleosols and foraminifera point towards a more southern position of the ITCZ during the MMCO compared to the modern era and a northward migration during the MMCT (Salazar-Jaramillo et al. 2022; Holbourn et al. 2010).

3 Methods

To simulate the MMCO's climate, I employ the IPSLs ESMs IPSL-CM5A2 and IPSL-CM6-LR using idealized Mid-Miocene boundary conditions. I carry out fully coupled and atmosphere-land simulations with fixed SSTs to investigate the role of land cover and parametrizations.

3.1 Models

3.1.1 IPSL-CM5A2

IPSL-CM5A2 is part of the CMIP5 model generation that presents a major step in climate modeling towards the previous CMIP3 generation, due to increased resolution and model physics complexity, which especially improved the ability to model regional climates (Gulizia and Camilloni 2015). IPSL-CM5A2 is a successor of IPSL-CM5A and was optimized for paleo-simulations through parallelization and optimized compatibility with paleoclimatological boundary conditions (Sepulchre et al. 2020a). It runs 3.8 times faster than IPSL-CM5A, simulating ∼100 model years per day. The atmosphere model used is LMDZ5, which simulates the atmosphere at $3.75° \times 1.875°$ resolution and 39 layers at a dynamic timestep of 2 min and a parameterization step of 30 min. The ocean model NEMO runs at 2° resolution and 0.5° in the tropics and at a timestep of 96 min. Further, it contains the land module ORCHIDEE, which is comprised of a hydrology and energy balance model (SECHIBA) that operates at a timestep of 30 min, and a vegetation, soil and carbon model (STOMATE) with a timestep of 1 d (Krinner et al. 2005). Its features an optional dynamical vegetation mode, that updates every model year (ibid.). Further, the model features a sea ice module (LIM2) and a marine biogeochemistry module (PISCES). All modules are coupled using OASIS. The model components, versions, and respective resolutions are given in Table 1. IPSL-CM5 uses a two-layer soil scheme consisting of two interacting bucket models (Krinner et al. 2005; Cheruy et al. 2020).

3.1.2 IPSL-CM6-LR

Like the entire CMIP6 ensemble, IPSL-CM6-LR exhibits a more accurate representation of the climate system than the previous model generation. One of the most pronounced improvements is the better representation of clouds, which leads to a more realistic estimate of the radiative budget (Boucher et al. 2020a). Further, it has a better representation of sea and air surface temperature and the ITCZ (Fan et al. 2020). The equilibrium climate sensitivity (ECS) was increased by ∼0.7 K to 4.75 ± 0.45 K compared to IPSL-CM5A (Boucher et al. 2020b).
IPSL-CM6-LR features improved versions of the modules included in IPSL-CM5A2. Its atmospheric component LMDZ6 runs at $2.5° \times 1.25°$ resolution, NEMO at 1° resolution and 1/3° in the tropics (Boucher et al. 2020a). The vertical atmospheric resolution is increased to 79 layers, which significantly improves atmosphere-surface interactions (Cheruy et al. 2020). It features a significantly improved ORCHIDEE version with eleven soil layers (compared to previously two layers) and more complex vegetation parameterization (De Rosnay et al. 2002; Boucher et al. 2020a). Further, the eddy diffusion and snow

scheme, as well as stratocumulus and gravity wave parameterizations, are significantly improved (Cheruy et al. 2020). A more detailed analysis of the capabilities of both modelsto represent the present climate, and the bias reductions in IPSL-CM6-LR is prsented in section 4.

Table 1: Characteristics of the model components of IPSL-CM5A2 and LMDZOR_v6.2.2 (IPSL-CM6-LR in atmosphere-vegetation configuration).

Earth System Component	Model	IPSL-CM5A2		LMDZOR_v6.2.2	
		Resolution	Version	Resolution	Version
Atmosphere	LMDZ	3.75° × 1.875° (lon-lat)	LMDZ5 Revision 6056	2.5° × 1.25° (lon-lat)	LMDZ6 Revision 3855
Land Surface	ORCHIDEE		Revision 7376		Revision 7086
Coupler	OASIS		OASIS3-MCT 2.0 Revision 4775		OASIS3-MCT 2.0 Revision 4775
Ocean	NEMO	Tripolar curvilinear ORCA2 2 ° and 0.5 ° in the tropics 31 vertical levels	Version 3.2	Tripolar curvilinear ORCA2 2 ° and 0.5 ° in the tropics Prescribed SSTs	—
Marine biogeochemistry	PISCES		PISCES-v2		—
Sea-ice	LIM2	ORCA2 grid 2 levels	cf. NEMO	ORCA2 grid 1 level, Prescribed	—

3.2 Simulation Strategy and Experiments

Even though it shows marked biases, IPSL-CM5A is one of the best-performing CMIP5 models in representing the complex processes of the SAMS (De Carvalho and Cavalcanti 2016). Therefore it is superior to its CMIP3 counterparts or Earth system models of intermediate complexity (EMICs) for the purpose of this study. At the same time, it is still efficient enough to perform equilibrating runs. With 13-16 model years per day in a comparable configuration, its CMIP6-counterpart IPSL-CM6-LR runs ∼7 times slower and uses proportionally more computing resources. Therefore, it is not feasible to perform equilibrating simulations with IPSL-CM6-LR for paleoclimatic conditions, which often takes thousands of model years and would take months to compute. Both models can be run in fully coupled mode (CPL) or in atmosphere-vegetation mode, which couples only the models LMDZ and ORCHIDEE (LOR). The LOR mode uses fixed SSTs and requires less computing time. Similarly, the dynamic vegetation (DV) is optional, and both setups run more efficiently with constant vegetation (CV). The model generations (5, 6) are used to distinguish the used model version in the simulation name.
This motivates my strategy to perform the equilibrating simulation in coupled mode and subsequent atmosphere-land simulations with IPSL-CM6-LR and IPL-CM5A2 in LMDZOR mode to get a more robust estimate of the monsoon dynamics during the MMCO.
The complete simulation plan starts with an initial, fully coupled simulation (CPL5-INIT) needed to initiate Mid-Miocene SSTs. These are used in a second, dynamical vegetation simulation to create the vegetation boundary conditions (LOR5-INIT). This is followed by the main, fully coupled simulation (CPL5-CV). To fully equilibrate the SSTs, I choose a duration of 3000 simulation years while the vegetation is kept fixed to increase the simulation speed. Subsequently, three more simulations are initiated using the SST pattern produced by CPL5-CV. First, I perform another dynamical vegetation simulation with IPSL-CM5 (LOR5-DV) to assess if the changed SSTs produce a significantly different vegetation distribution and climate. A second atmosphere-vegetation simulation using IPSL-CM6-LR, forced with CPL5-CVs SSTs and vegetation (LOR6-CV), is run to inves-

tigate climate differences purely caused by resolution and parameterization differences. At last, the dynamical vegetation simulation LOR6-DV investigates how the vegetation behaves in the new model version and allows to investigate possible atmosphere-vegetation feedbacks while also using CPL5-CVs SST as boundary conditions. Instead of performing an additional 'LOR5-CV' simulation, CPL5-CV is taken as reference simulation with fixed vegetation compared to LOR5-DV. The entire simulation scheme is illustrated in Figure 3.

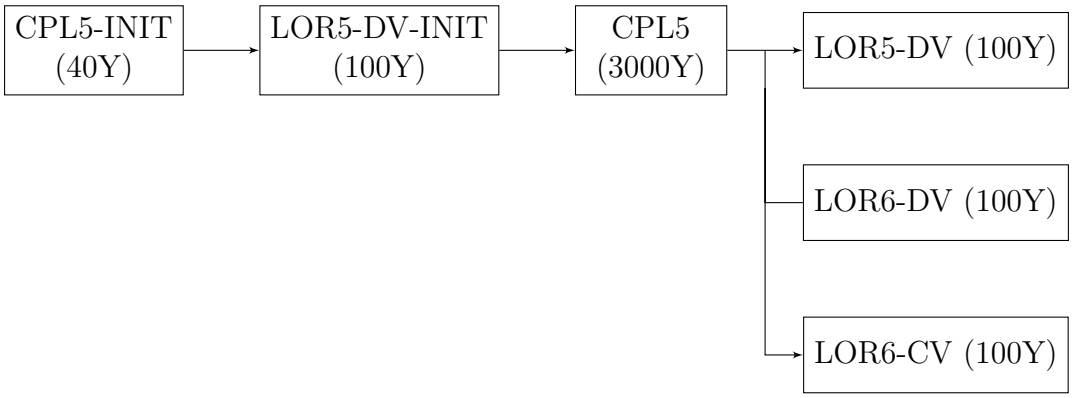

Figure 3: Sequence of performed MMCO simulations.

3.3 Boundary Conditions

In the past years, the Miocene Model Intercomparison Project (MioMIP; Burls et al. 2021) has contributed to the comparison of available MMCO reconstructions and standardization of model experiments. In order to ensure comparability to existing simulations and ensure comparability to ongoing modeling efforts, I perform the MMCO simulations with standardized boundary conditions and forcings wherever possible.

3.3.1 GHG and Orbital Forcings

The concentrations of GHG required to achieve radiative forcings sufficient to reproduce high MMCO temperatures have been studied in MioMIP1 (ibid.). Simulations with 3×PI pCO_2 produced the best results, keeping pCH_4 and pNO_2 at preindustrial levels.
Accordingly pCO_2, I assume a concentration of 840 ppm (3×PI), for pCH_4 and pNO_2 preindustial concentrations of 790 ppb and 275 ppb. The exact concentrations of those trace gases are difficult to estimate due to missing proxies. The high pCO_2 levels are supported by a number proxies for pCO_2 levels of over 800 ppm (Rae et al. 2021; Steinthorsdottir et al. 2021a). The solar constant is set to 1365 $W\,m^{-2}$, following Miocene reconstructions and other studies (Ring et al. 2022; Herold et al. 2011).
During the 2.25 Ma period of the MMCO, the Earth underwent several full orbital cycles (Steinthorsdottir et al. 2021b). The orbital parameters can affect monsoon intensity and length through variation of the variation of incoming radiation (Braconnot et al. 2007). Since I am interested in isolating the effects of changes in other forcings,the orbital parameters are kept fixed to the present-day values.

3.3.2 Paleogeography

For the topography and bathymetry, I use the reconstruction by Herold et al. (2011), which was also used in MioMIP1. The reconstruction was created for 15 Ma and is assumed to be representative of the MMCO. The reconstruction is very similar to reconstructions like the one by Frigola et al. (2018) for 14 Ma, which differs mainly in a more advanced tectonic convergence in the Himalayas. The used reconstruction contains all seaways and orographic features discussed in section 2.2.1, and is displayed in Figure 4.

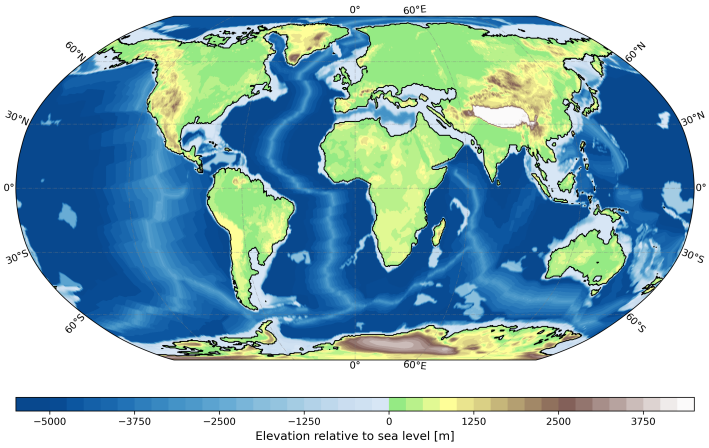

Figure 4: Relief reconstruction by Herold et al. (2011) used as topographic and bathymetric boundary condition for the MMCO simulations.

In a preparatory step, the relief file was examined for compatibility with the model. After regridding it to the model resolution, ocean gateways that are thought to have played a significant role in ocean dynamics were made sure to be two grid points wide and sufficiently deep to allow for dynamic advection within the ocean model. Sub-sea level grid cells on land were removed from the ocean, and a routing scheme that codes which ocean runoff is directed was applied to the land surface.

3.3.3 Prescribed Ice Sheet

The topography reconstruction includes an early east-antarctic ice sheet. Since the model uses a fixed antarctic ice sheet, I created a land-ice mask from the topography reconstruction (cf. Fig. 5). In a simple, altitude-dependent accumulation-ablation heuristic, I consider all areas above 1400m to be glaciated, which compares well to existing reconstructions (ibid.). This resulting glaciated antarctic area is $3.7 \times 10^6\,\mathrm{km}^2$, which is about 27% of the modern $13.9 \times 10^6\,\mathrm{km}^2$ (Fretwell et al. 2013). Ice shelves are not prescribed since summer SSTs are considered too high to sustain them. Sea ice is not initially assumed present but is free to develop.

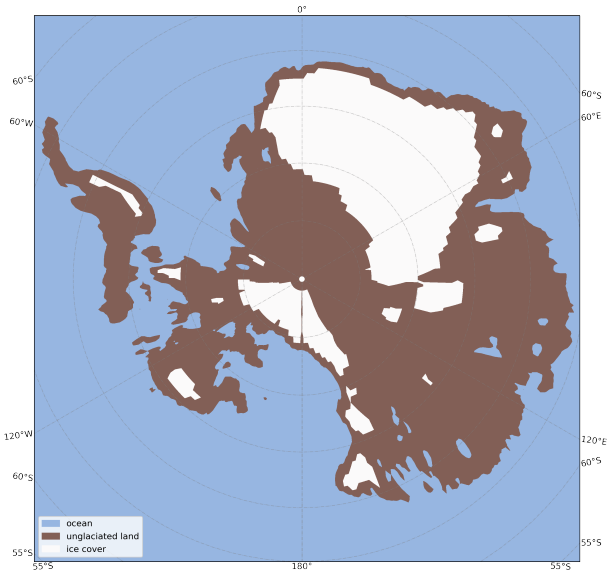

Figure 5: Antarctic ice sheet reconstruction used for the MMCO simulations.

3.3.4 Vegetation Map

The ORCHIDEE model features thirteen plant functional types (PFTs), which represent different types of land cover (15 PFTs in ORCHIDEE2.0, cf. Tab. 2). To match the periods' vegetation, I exclude the C4 and cropland PFTs (cf. sec. 2.2.3). LMDZOR6 features three different C3 grass types (cf. Tab. 2), but I sum up their coverage after the simulation for better comparability with IPSL-CM5A2. ORCHIDEE can run both with a prescribed PFT map as well as dynamically evolving vegetation distribution. The plant functional types have individual parameterizations for interacting with the atmosphere, radiation, and hydrological and nutrient cycles and cover a certain percentage of a grid cell. Photosynthesis is considered in a singe-leaf scheme, where woody biomes have several vertical levels and partially show deciduous behavior (Krinner et al. 2005).

Table 2: List of the PFTs considered for the MMCO. (*) Only present in LMDZOR5, IPSL-CM5A2; (†) Only present in LMDZOR6. All vegetation maps combine temperate and boreal PFTs for better readability.

N	Vegetation Type
1	Bare soil
2	Tropical broadleaf evergreen tree
3	Tropical broadleaf deciduous tree
4	Temperate needleleaf evergreen tree
5	Temperate broadleaf evergreen tree
6	Temperate broadleaf deciduous tree
7	Boreal needleleaf evergreen tree
8	Boreal broadleaf deciduous tree
9	Boreal needleleaf deciduous tree
10a*	C3 Grass
10b†	Natural Grassland (C4)
11†	Tropical Natural Grassland (C3)
12†	Boreal Natural Grassland (C3)

Since the MMCO continental distribution and plants differed from modern vegetation, existing vegetation maps cannot be used as boundary conditions for my simulations. Also, the vegetation map has to match the available vegetation types of ORCHIDEE. As discussed in section 3.2, I perform a short (40-year) coupled simulation to obtain an ad-hoc MMCO-SST map and use these warmed, unequilibrated SSTs to initiate a 100-year LMDZ-ORCHIDEE (atmosphere-land) simulation dynamical vegetation mode to create an ad-hoc mid-Miocene vegetation distribution (LOR5-INIT). Crops and modern C4-Grasses are excluded from the dynamical vegetation model to better represent the MMCO flora. The average of the last ten years of the modeled vegetation is taken as the vegetation boundary condition for the coupled Miocene simulation.
A time series of the vegetation distribution (cf. Fig. 6a) shows initially unvegetated land and a quick spread of C3 Grasses in the first ten years, followed by a slower onset of all woody vegetation. Within 20 years, the quick expansion is finished, followed by a slow increase of woody vegetation, phasing out after about 80 years. Figure 6b shows the dominant PFT for each grid cell, averaged over the last ten years of the simulation. The spatial distribution of PFT cover shows reflects local climates like deserts and coastal influences. Also, it shows characteristics of the MMCO, like vegetation in Antarctica and the Neogene onset of deserts. In South America, the PFT map includes tropical forests in the low latitudes, an unvegetated Atacama desert, rainforests in the low latitudes, grasslands in the subtropics, and warm-temperate forests in southern South America.

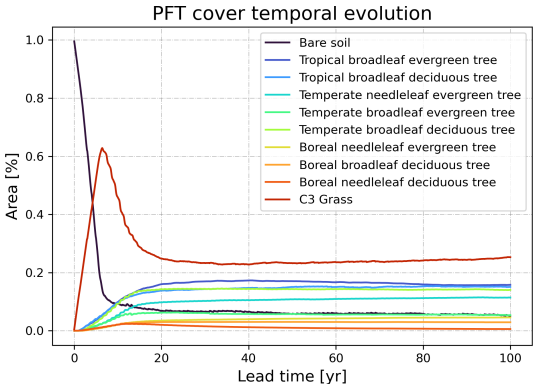

(a) Temporal evolution of proportionate land area covered by individual PFTs.

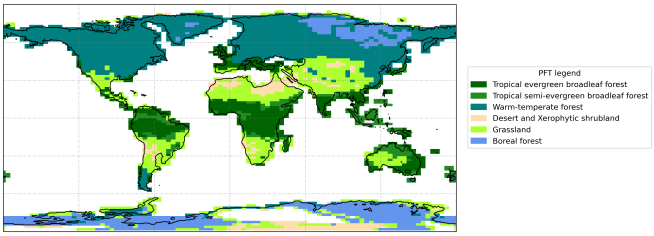

(b) Maximum vegetation type for each grid cell.

Figure 6: Vegetation map created by LOR5-DV-INIT as boundary conditions for the coupled MMCO simulation CPL5-CV. Left: Temporal evolution of the global vegetation fraction for each PFT; Right: Map of the dominant PFTs averaged over the last 20 simulated years.

Although initiated with inequilibrated SSTs, this vegetation distribution is considered to give a better representation of the MMCO vegetation than a simple zonal distribution could provide, when compared to the vegetation proxies by Pound et al. (2012).

3.4 Analysis

3.4.1 Metrics and Tools

There are several quantitative tools like indexes and thresholds for features of the SAMS, based on either precipitation, winds, OLR or all of them, quantifying exact onset and demise and climatological pattern of the SAMS (Correa et al. 2021; Gan et al. 2005; Da Silva and De Carvalho 2007). Since the indexes were designed based on assumptions of modern climate, they don't necessarily translate well into Miocene climate.Therefore, I rely on a more qualitative analysis of the SAMS. I follow the phenomenological analysis of Espinoza et al. (2020) to characterize the presence and dynamics of a SAMS, assessing the four dominant features that constitute a positive SAMS phase. This includes the presence of the BH at 200-300 hPa, the formation of a SACZ, the presence of the SALLJ and a high tropical Atlantic SST gradient before the onset of the SAMS (ibid.). The SALLJ strength is assessed in terms of mean DJF 850 hPa northwesterly wind east of the low to mid-latitude Andes, as well as the vertical wind shear between 850 hPa and 700 hPa (cf. ibid.). The BH is assessed through the 200 hPa pressure and wind field, following (cf. Lenters and Cook 1997). The SST gradient is measured between 60°W–30°W and 5°N–25°N, and 30°W–0°W and 5°N–25°N, following Giannini et al. (2004). The SACZ position and intensity is assessed through the OLR and CAPE (cf. Rosa et al. 2020). Further, I investigate the convective tropical precipitation by constraining the ITCZ position through the criterion by Braconnot et al. (2007).

$$\hat{w}_{ITCZ,S}(lon) = \frac{\sum_{y=lat(pr_{max})}^{30°S} pr(y) * y}{\sum_{y=lat(pr_{max})}^{30°S} pr(y)} \tag{1}$$

This criterion, which calculates the center of mass of total precipitation between the troical precipitation maximum and 30° latitude on each hemisphere, gives an estimate of the width of the ITCZ south, and analogous north, of its maximum. To capture other tropical convective phenomena like the ITCZ, I distinguish large-scale and convective precipitation that are separately parameterized within the models. Further, I investigate the outgoing long-wave radiation (OLR), which is a strong indicator of the monsoon activity (Dutton et al. 2000; Carvalho et al. 2004) due to its susceptibility to cloud cover (K. Zhang et al. 2017). The seasonal means of the periods December, January and February (DJF) and June, July and August (JJA) are assumed representative for the positive and negative SAMS phase. This is a common practice when investigating the SAMS since the seasons coincide well with the two poles of the SAMS, and the onset during September, October and November (SON) and decline during March, April and May (MAM) show more transient climatic patterns (Espinoza et al. 2014; Vera et al. 2006b). Further, I conduct an analysis of the regional and seasonal water budget. For this purpose, I define seven climatological region masks over South America, based on common seasonality in present-day hydrology (cf. Fig. 7).

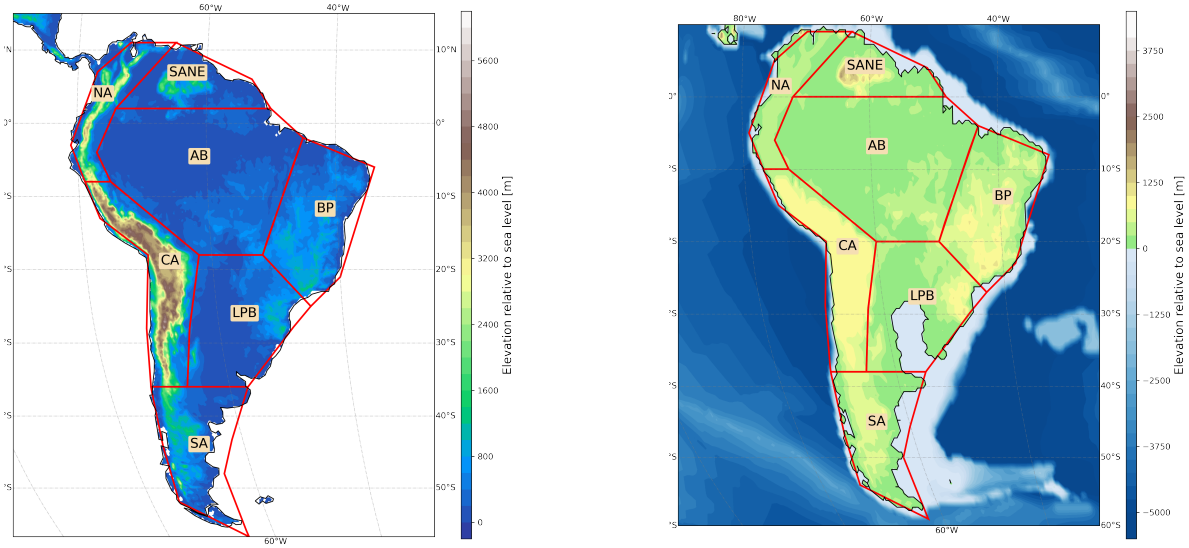

Figure 7: The seven subregions defined for regional analyses: Northern Andes (NA), North East South America (NESA), Central Andes (CA), Amazon Basin (AB), La Plata Basin (LPB), Brazilian Plateau (BP) and Southern South America (SSA). The left figure shows their position in the present day geography, the right figure the regions during the MMCO. The relative shift amounts to Δx=-2° and Δy=2°.

North East South America (NESA) covers the regions of today's Orinoco Basin and Guyana Shield, whose seasonal precipitation is against the SAMS with a dry period in austral summer and a precipitation maximum in JJA. The adjacent northern Andes (NA) region covers the low-latitude Andes and west coast of South America, which lie in between the SAMS poles and have a complex year-round precipitation. To the south of NA are the considerably higher Central Andes (CA), which correspond to the region of the Andes, that was already over 1000 m high during the MMCO. Next, there is the Amazon Basin (AB), La Plata Basin (LPB), and Brazilian Plateau (BP), which show

in-phase precipitation patterns but are defined as separate regions due to their different vegetation and moisture sources. All land below 38°S is part of Southern South America (SSA), which is not directly affected by the main monsoon circulation today.
The hydrology budget of the regions is assessed through a simple P-E (precipitation - evapotranspiration) evaluation, which can be a valuable tool to investigate past hydrology and vegetation feedbacks in monsoon regions (Braconnot et al. 1999). Globally, P-E must be zero under the conservation of water. Hence, spatio-temporal anomalies indicate water import or export (Elbaum et al. 2022).

3.4.2 Data

As a reference data set for the MMCO period, I use a preindustrial (PI) 6000y equilibrium simulation that had been previously performed using IPSL-CM5A2 and was provided by the IPSL, as well as preindustrial hydrological data for IPSL-CM6-LR from the CMIP6 data release. To analyze the model bias, I use historical simulations (1981-2010) from IPSL-CM5A2 and IPSL-CM6-LR, provided by the Copernicus data storage (CDS). The ERA5 reanalysis product is considered accurate enough to qualify as an observational reference for this period. The product is known to have biases in resolving the short-time hydrology in South America. However, since I mainly consider monthly averages, the reanalysis product is considered sufficiently accurate compared to other data sets like GPCP (Nogueira 2020). Since the data sets have different resolutions, they were regridded to a 1×1 degree resolution for better comparability. For validation, I employ the SST data sets by Burls et al. (2021), and the qualitative proxies as discussed in section 2.2, as well as the vegetation proxies by Pound et al. (2012).
All simulations were performed on the IRENE-AMD partition of the TGCC super-computing center and post-processed on the LSCE's cluster. For the 3000Y fully coupled simulation (CPL5-FV), the years 1200– 1350 yr are chosen as reference period. The reason for this is an anomalous increase in downward shortwave radiation caused by an imbalance between parameterization timestep and dynamic timestep, resulting in a $2\,\mathrm{W\,m^{-2}}$ positive radiation bias and significant temperature bias (cf. Figure 8). The error was produced when the timestep was increased due to instabilities in the model run, and the model behavior had not been attributed to this error until after the simulation ended. The period 1200–1350 yr is the period closest to model equilibrium. The cooling after the short period with high radiative forcing and temperature between the years 870 and 970 shows that the equilibrium is stable towards slightly higher radiative forcing episodes. The remaining radiative imbalance of 1 W has been previously observed for deep-time paleoclimate simulations such as the Cretacious (Sepulchre et al. 2020b), while there is no imbalance in the preindustrial, which the model was tuned upon. Since the imbalance in constant, the model is considered to be in equilibrium at a TOA net radiation flux of $\sim 1\,\mathrm{W\,m^{-2}}$.

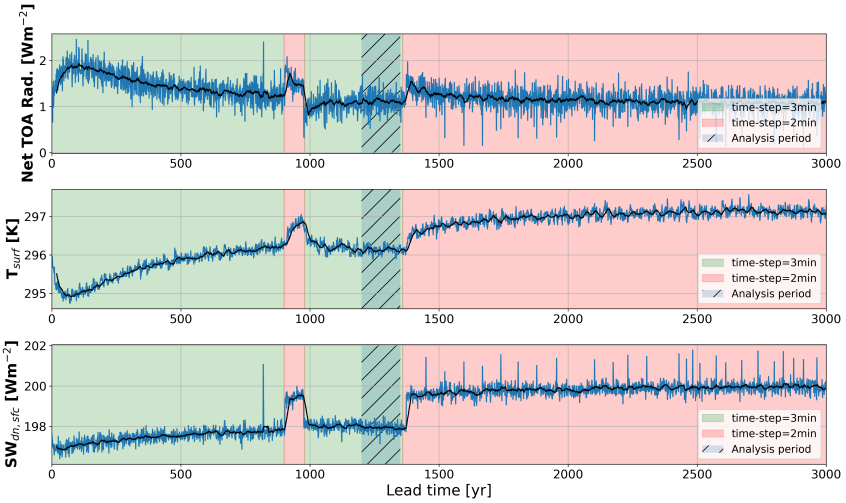

Figure 8: Key variables to track the simulation course (net radiation balance at top of atmosphere (TOA), surface temperature, and downwelling shortwave radiation). The shading shows period with correct (green) and incorrect (red) dynamics-parameterization timestep-ratio. The hatched area marks 1200-1350 yr, which was chosen as reference period.

4 Assessing the South American Model Biases

Climate models have difficulties in reproducing certain aspects of the Climate System. It is essential to understand the existing biases to make an educated estimate of how they affect a simulated paleoclimate. Therefore, I will review known model biases and their sources in this section and investigate the capabilities of the used models in reproducing the main climatic features of the SAMS.

A major bias that continues to persist in CMIP5 and CMIP6 and that is present in both IPSL models is the 'double ITCZ bias', meaning the models simulate two separate convection bands along the tropics due to a pacific cold-tongue (Li and Xie 2014). The bias is connected to biases in tropical precipitation and surface easterly winds that arise from deficient atmosphere-ocean interaction (ibid.). Stouffer et al. (2017) identified five more major biases in CMIP5 models. These include a bias in the Walker circulation, a poor representation of tropical and subtropical clouds, an overly deep tropical thermocline, a warm and dry bias of summer land surfaces, and an insufficient reproduction of the location of the southern-hemispheric jet. These biases are present in IPSL-CM5A and are reduced in IPSL-CM6-LR (Boucher et al. 2020a). Further, the processes in Eastern Boundary Upwelling Systems are not sufficiently resolved, leading to reduced upwelling and subsequently elevated SSTs in these areas (Q. Zhang et al. 2023). Interestingly, all of the named biases affect the South American climate, which stresses the importance of understanding their effect on the simulated SAMS. The bias in the Walker circulation has been shown to contribute to the Amazon dry bias and, together with the deep thermocline, affect the ability to capture the ENSO events correctly (Stouffer et al. 2017).

In the modern era, most climate models, including those used in this study, show a dry bias over the Amazon, especially during the austral winter. This bias has been continuously reduced between the model generations but persists today (Gulizia and Camilloni 2015). Most notably, IPSL-CM5A2 exhibits a dry bias over the entire continent during DJF and a dipole during JJA, with a too-dry northern Amazon and too-wet southern Amazon (cf. Fig. 9). IPSL-CM6-LR reduces the dry bias significantly, but a dry bias in the core Amazon persists. Further, IPSL-CM6 captures the seasonality of precipitation better and improves the dry bias in the dry season found in many regions (Cheruy et al. 2020). Both models have difficulties simulating the Atlantic ITCZ. As can be seen in Figure 9, IPSL-CM6-LR shows a southern displacement, leading to anomalous precipitation at the Brazilian high and a dry bias over the tropical north Atlantic. In contrast, IPSL-CM5A2 shows a more complex error with a double ITCZ in DJF and shortcomings in reproducing its seasonal cycle (Sepulchre et al. 2020a). The precipitation bias is connected to the temperature bias, revealing mostly elevated temperatures in places that show a dry bias. This hot bias can be most prominently seen in the east to central Amazon, where temperatures exceed the observations by more than 6° year-around (cf. Fig. 9). IPSL-CM6-LR shows an almost unilateral reduced temperature bias. The main difference to ERA5 is a temperature pattern caused by unresolved topography (see Andes, Brazilian Plateau). Eastern Amazonia continues to display a warm bias, although the amplitude is significantly reduced.

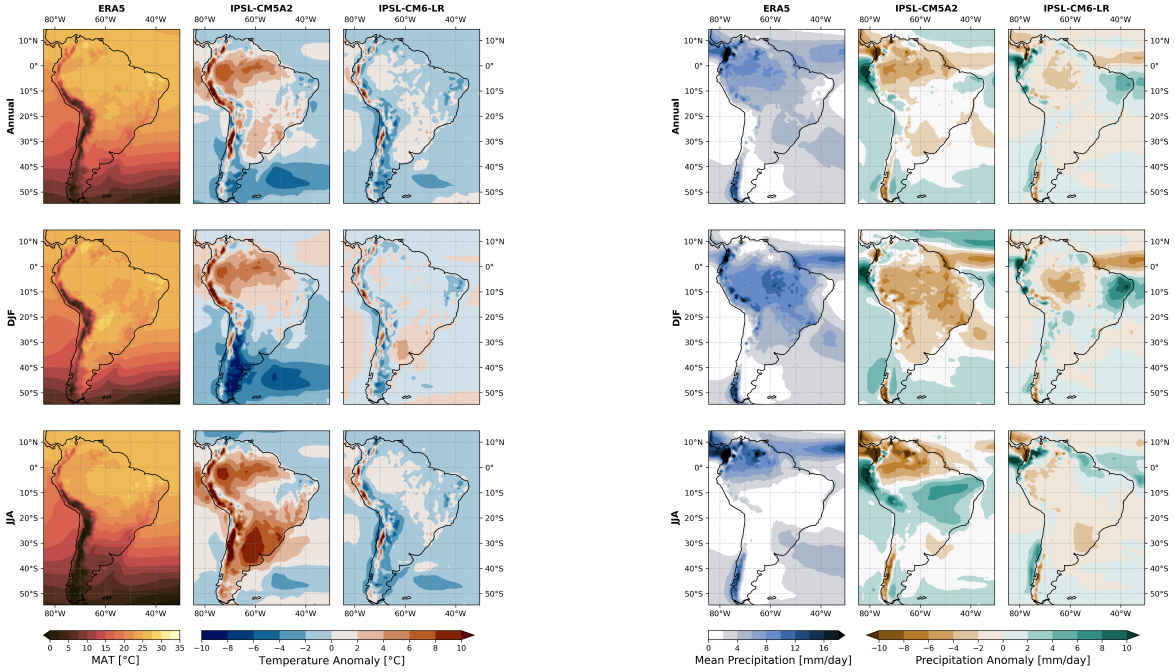

Figure 9: Mean annual and seasonal temperature and precipitation in South America in the ERA5 reanalysis dataset (left), as well as the observed anomaly for IPSL-CM5A2 (middle) and IPSL-CM6-LR (right). The reference period for the reanalysis and historic simulations is 1981-2010.

4.1 Cloud Representation

One reason for the tropical cloud bias in IPSL-CM5A2 is its tuning. In order to overcome an initial cold bias, a convection parameter was adjusted to reduce convective clouds and thus increase the downward SW radiation. This leads to a better overall temperature representation but worsens the biases in the Amazon (Sepulchre et al. 2020a). The reduced convection leads to too little cloud formation over the Amazon, increasing the downwelling short-wave radiation (cf. Fig. 10), which leads to anomalous warming enhanced by a too-positive long-wave cloud radiative forcing (CRF) (ibid.). At the mid-latitudes, on the other hand, low-level clouds are too reflective, leading to a negative SW CRF. Yin et al. (2013) identify this positive surface SW radiation bias due to underestimation of cloudiness to be the critical factor for the precipitation bias in CMIP5 models, including IPSL-CM5A, a bias that is even slightly worsened in IPSL-CM5A2. The fact that biases can often be jointly diminished (Mueller and Seneviratne 2014) explains how the improvement in cloud representation and the radiation budget can improve multiple variables like temperature, precipitation, and evaporation between IPSL-CM5A2 and IPSL-CM6-LR.

4.2 Winds and Orography

IPSLCM5A2 shows a general bias of the subtropical jets positioned at too low latitudes (Sepulchre et al. 2020a). This leads to a too-high extension of the westerlies over South America. The jet position is significantly improved in ISL-CM6-LR, which is attributed to its significantly higher vertical resolution (Boucher et al. 2020a). Further, the Atlantic easterlies are underestimated in IPSL-CM5A2, which leads to a decreased westward humidity transport from the Atlantic, the primary source of South American moisture (Sepulchre et al. 2020a; Espinoza et al. 2014). The improved resolution of IPSL-CM6 also leads to a better representation of the Andean orography and interaction with the South American wind systems. On top of the higher resolution, it uses a Subscale Grid Orography Scheme (SSO) to parameterize unresolved properties like orographic blocking and gravity wave generation (Cheruy et al. 2020). These advancements can be seen in the low-level zonal wind pattern, which shows anomalous westward wind through the equatorial Andean Cordillera (cf. Fig. 11) between 8°S and 2°S. In IPSL-CM5A2, this 'leakage' amounts to $1.5 \times 10^8\,\mathrm{kg\,s^{-1}}$ of Amazonian moisture during the wet season, which corresponds to 30% of the Amazon rainfall rate during DJF, overestimating the westward moisture flux in this region by a 600%. In IPSL-CM6-LR, the moisture export is only elevated by 44%. This draws humidity out of the precipitation-evapotranspiration cycle over the Amazon and reduces the moisture transport to southeast South America. Junquas et al. (2016) has previously demonstrated that a complete removal of the Andes leads to a wetter equatorial East-Pacific and reduces moisture transport to the South American subtropics.

4.3 SAMS Features

Both models represent all dominant SAMS features. During DJF, both models show a Bolivian High, although in IPSL-CM5A2, it is slightly displaced to the northwest (cf. Fig. 12). IPSL-CM6-LR shows the BH at its correct position but slightly zonally elongated,

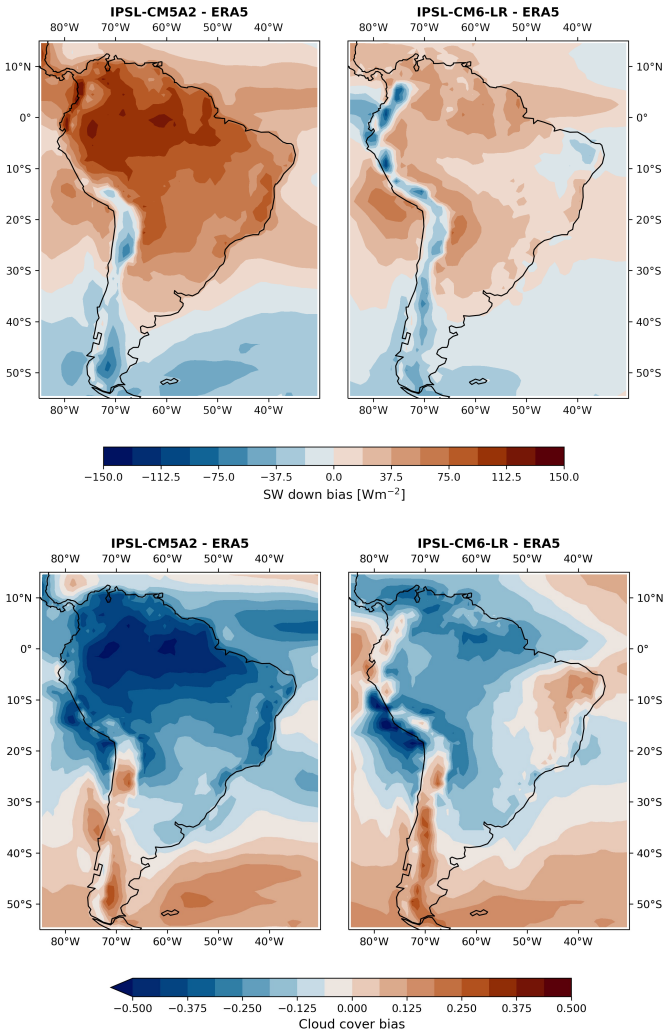

Figure 10: DJF cloud cover and shortwave-downwelling radiation biases for historical IPSL-CM5A2 and IPSL-CM6-LR simulations. The reference data is the ERA5 reanalysis (1980-2010).

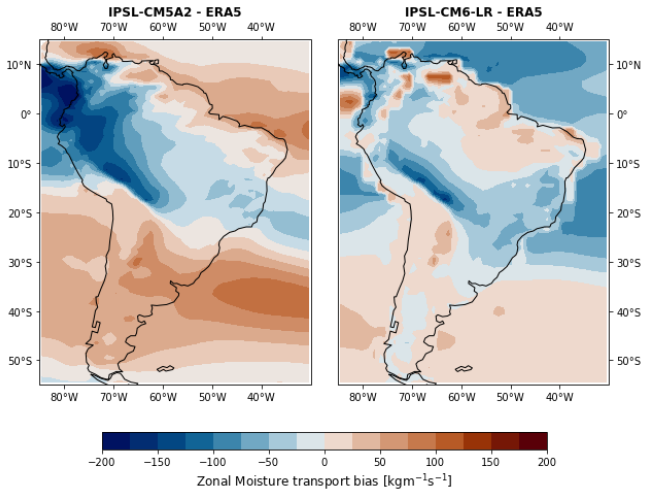

Figure 11: DJF zonal moisture transport anomaly with respect to ERA5.

which has previously been found by (Lenters and Cook 1997). IPSL-CM6-LR also shows a more realistic continental low-level wind pattern, likely due to the more accurate representation of orography. This leads to a higher estimate of northwesterly winds east of the central Andes, associated with the SALLJ, and an overall closer match with the wind pattern exhibited in ERA5 (cf. Fig. 12).

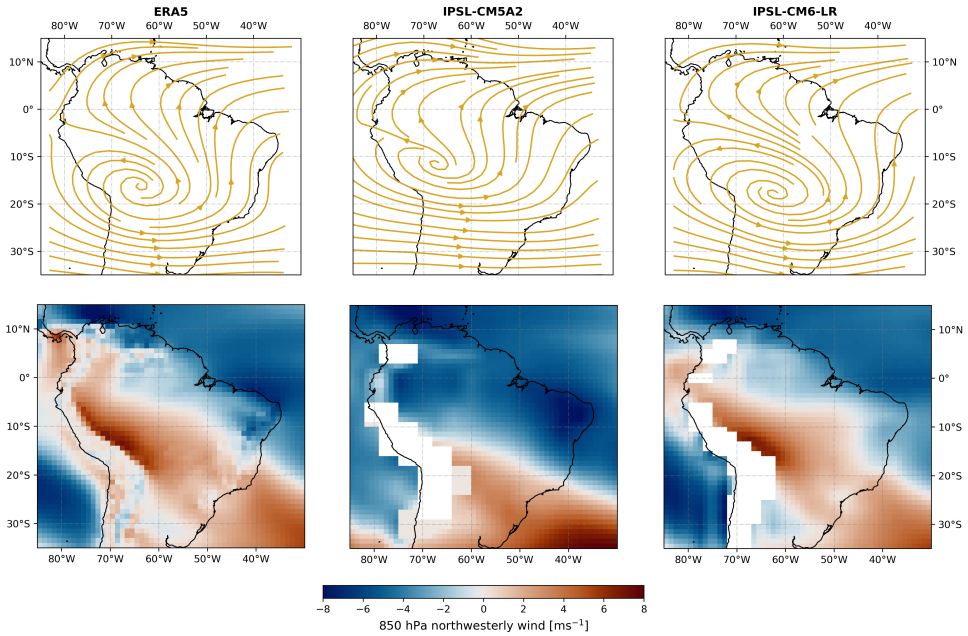

Figure 12: 200 hPa stream plot and 850 hPa northwesterly winds pattern in DJF, showing the respective representations of the BH and SALLJ for IPSL-CM5, IPSL-CM5-LR and ERA5 in the historic period 1980-2010.

5 Results

5.1 The MMCO Climate of IPSL-CM5A2

The fully coupled MMCO simulation (CPL5-CV) shows a mean air temperature 8.9±0.1 K higher compared to the pre-industrial reference simulation. Globally, the simulation shows enhanced warming over land and the polar regions (cf. Fig. 13). Regions that are glaciated in the pre-industrial show a strong temperature increase of over 20 K. Global precipitation is increased by $0.65 \pm 0.01\,\mathrm{mm\,d^{-1}}$, which corresponds to a 24% increase. The strongest increases are seen in tropical South America and Oceania. Precipitation is reduced over South Asia, the Subtropical Americas, and central Africa.

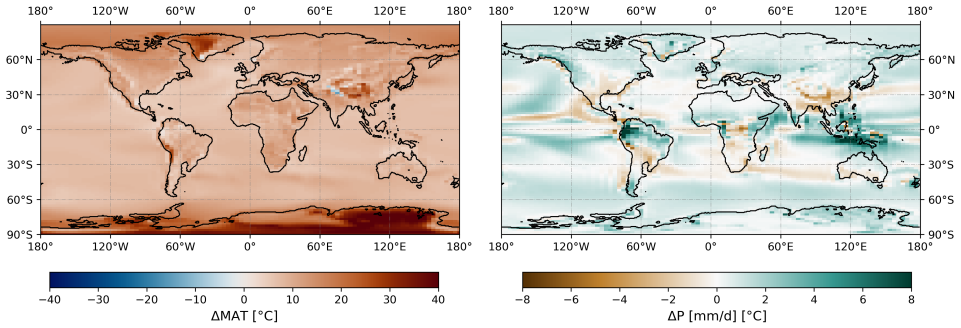

Figure 13: Global changes in temperature and precipitation in CPL5-CV (MMCO) compared to the preindustrial IPSL-CM5A2 reference simulation.

The zonal wind distribution shows a shift towards higher latitudes. This results in a broadening and weakening of the trade winds, as well as a poleward shift of the subtropical westerlies and strengthening of the upper-level westerlies (cf. Fig. 14). The southern-hemispheric polar easterlies are slightly weakened compared to the PI.

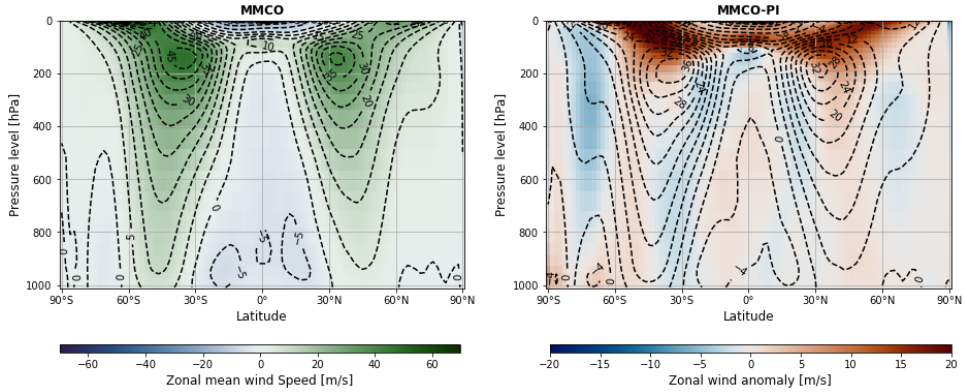

Figure 14: Left: Zonally averaged wind velocities of CPL5-CV. Right: Differences in zonal wind of CPL5-CV compared to the PI reference simulation, with PI wind velocities as contour lines.

The ITCZ extension and position, shown in Figure 15, is similar to the PI but shows some regional variations. Over the Western Indian Ocean, the summer ITCZ shows a more northern position over the East African Coast but a more southern position near

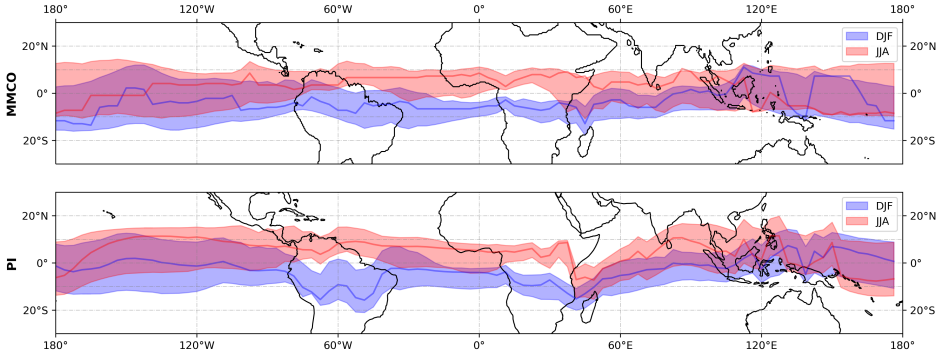

Figure 15: Mean summer and winter position of the ITCZ during summer and winter. Blue and red lines show position of mean maximum precipitation, shaded areas show extent (following Braconnot et al. (2007)). Upper image: CPL5-CV (MMCO); Lower image: PI IPSL-CM5A2 reference simulation.

Asia. In the West Pacific, the southern branch of the erroneous double ITCZ is weakened during summer, leading to a more northward modeled position than the winter ITCZ. Over South America, it shows a more northern position, which is enhanced with respect to the relative position of the land by the two degree southward shift of the South American continent.

5.1.1 South American Climate and Hydrology

The mean large-scale seasonal South American circulation shows a stronger seasonality than the modern monsoon circulation. Especially the lower-level JJA circulation shows a much higher extension of westerlies to low latitudes (cf. Fig. 16), compared to present-day (cf. Espinoza et al. 2020). The upper-level DJF circulation shows stronger easterlies, reaching higher latitudes, while the upper-level JJA circulation remains relatively similar to the PI. The subtropical high-pressure systems over the Atlantic and Pacific show a south-eastern migration, weakening the influence of the South Atlantic high on the tropical South American circulation.

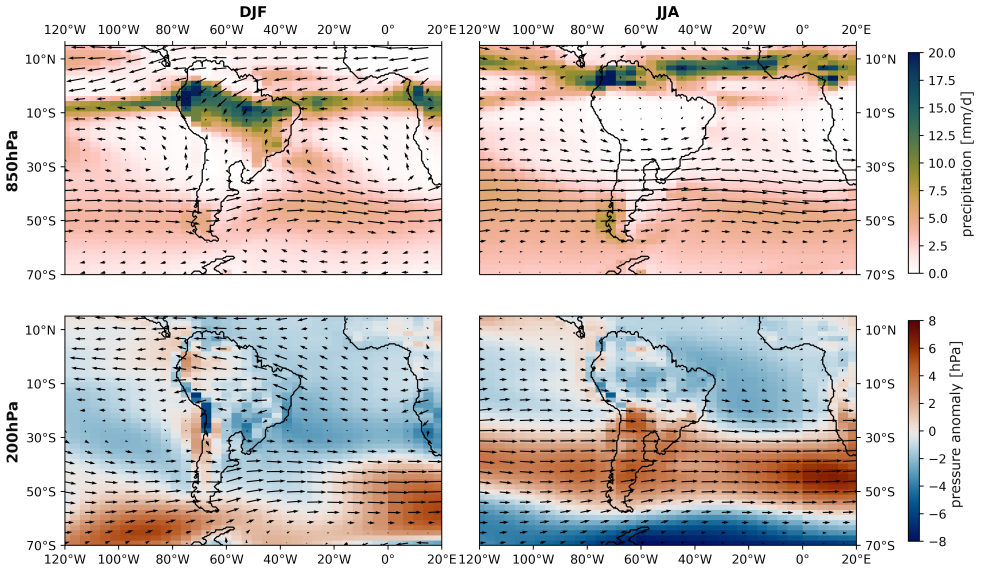

Figure 16: Mean 850 hPa and 200 hPa wind fields for DJF and JJA, as simulated by CPL5-CV. Shading shows seasonal mean precipitation, as well as the mean pressure anomaly compared to the PI reference simulation for DJF and JJA.

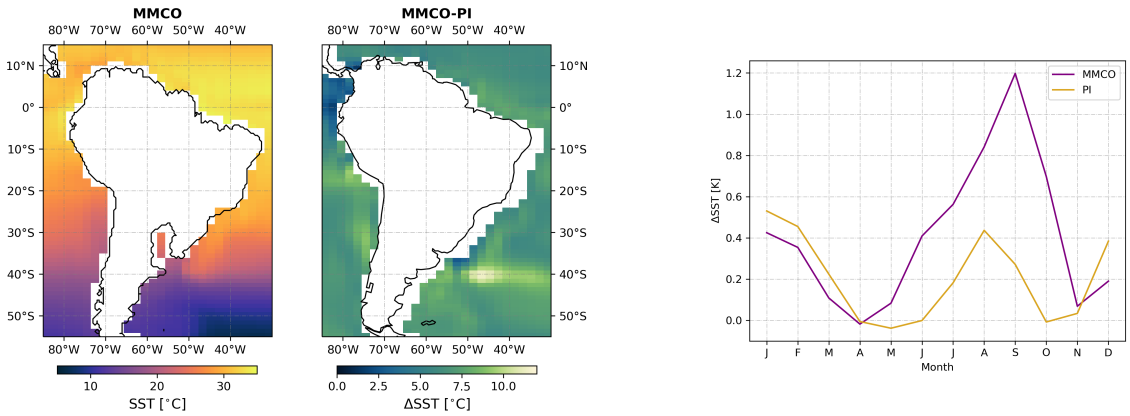

Figure 17: Left: SST maps of the IPSL-CM5A2 simulation CPL5-CV (MMCO) and the SST difference compared to the preindustrial reference simulation near South America; Right: monthly averaged tropical Atlantic SST gradient (60°W–30°W and 5°N–25°N minus 30°W–0°W and 5°N–25°N) simulated in CPL5-CV and the preindustrial reference simulation.

CPL5-CV shows a weakened ocean overturning circulation (closer discussed in Ch. 6), which, combined with the low-level winds, leads to a change in ocean currents and the SST pattern near South America. A warming of more than 11 K can be observed off the southeast South American coast, where the Brazil current extends ∼2.5° to the south. Further, over-proportional warming is observed along the Humboldt current, while the equatorial East Pacific near the CAS shows a disproportionately low warming of only 2 K (cf. Fig.17). The tropical Atlantic SST gradient associated with the onset of the positive SAMS phase (cf. Ch. 3) increases threefold from May to November, showing a distinct peak in September, which is one month later than in the PI. However, no delay in the seasonal precipitation can be seen in CPL5-CV.

5.1.2 SAMS features

The other three dominant SAMS features, BH, SACZ, and SALLJ, (Espinoza et al. 2020) are all present in the MMCO simulation but vary in position and strength. There is still a northwesterly band of cloudiness and convection associated, as OLR and CAPE show (cf. Fig. 18), but it is elongated and shows its intensity maximum over the southern tropical Atlantic instead of SESA. The main convective activity occurs in the Amazon, shifting equatorward and broadening. This convection connects with the SACZ to a broad, north-east oriented tropical convective belt with a dipolar structure, peaking in the West Amazon and southern Tropical Atlantic. The simulation further shows the presence of a Bolivian high, centered at 12°S and 60°W and strengthened compared to the PI.

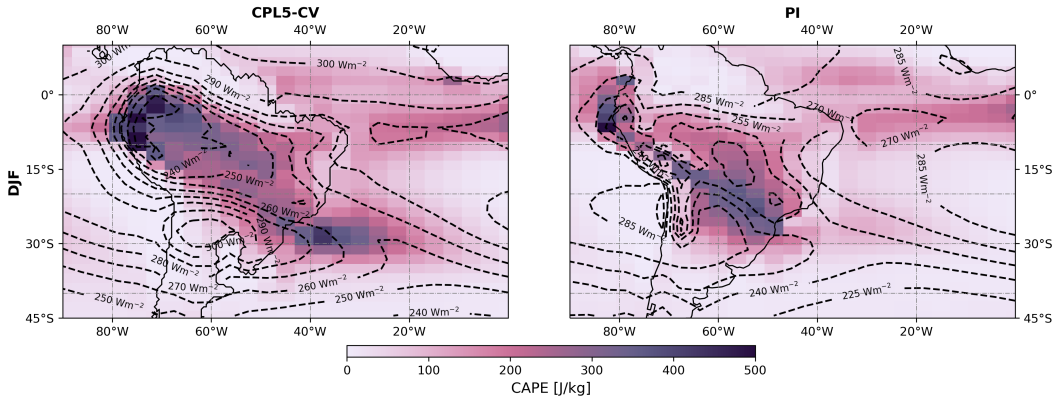

Figure 18: Mean DJF levels of Convective Available Potential Energy (CAPE) for the MMCO and PI. The corresponding levels of outgoing long-wave radiation (OLR) are shown as contour lines.

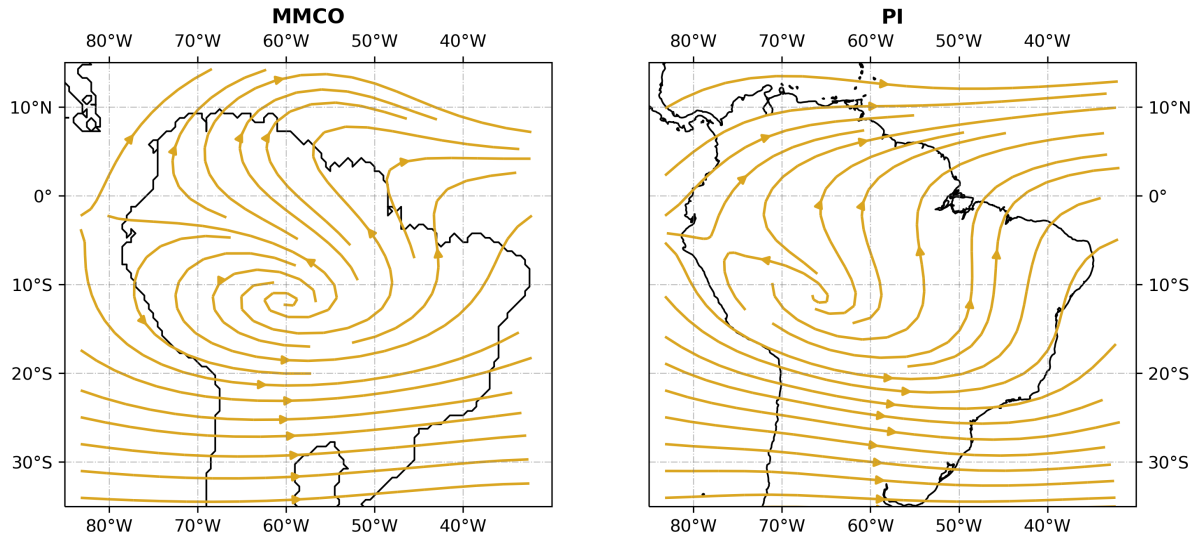

Figure 19: Streamplot of the 200hPa winds during DJF, revealing the modeled position of the Bolivian High during the MMCO.

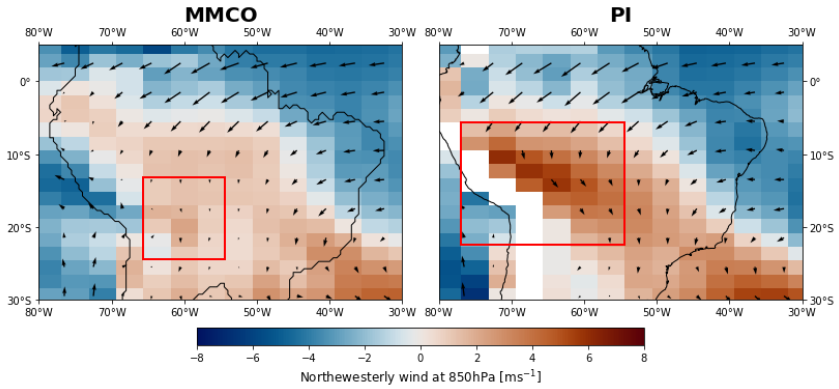

Figure 20: Northwesterly 850 hPa winds in central South America in CPL5-CV (MMCO) and its preindustrial IPSL-CM5A2 reference simulation. Red boxes show the areas of highest SALLJ.

The mean 850 hPa circulation shows decreased northwesterly wind speeds (up to 2.2 m s^{-1} in the SALLJ regime (up to 6.0 m s^{-1} in PI), but the vertical wind shear in the northwesterly direction in the SALLJ-region between 850hPa and 700hPa is more pronounced during the MMCO (MMCO: $\sim$ 6.6 m s^{-1}, PI: 4.7 m s^{-1}). Notably, the mean 850 hPa wind is northwesterly, considering the strong vertical wind shear. This speaks for the presence of SALLJ events, but they are thought to be weaker, judging by the reduced mean wind speeds.

5.1.3 Continental Patterns of Hydrology

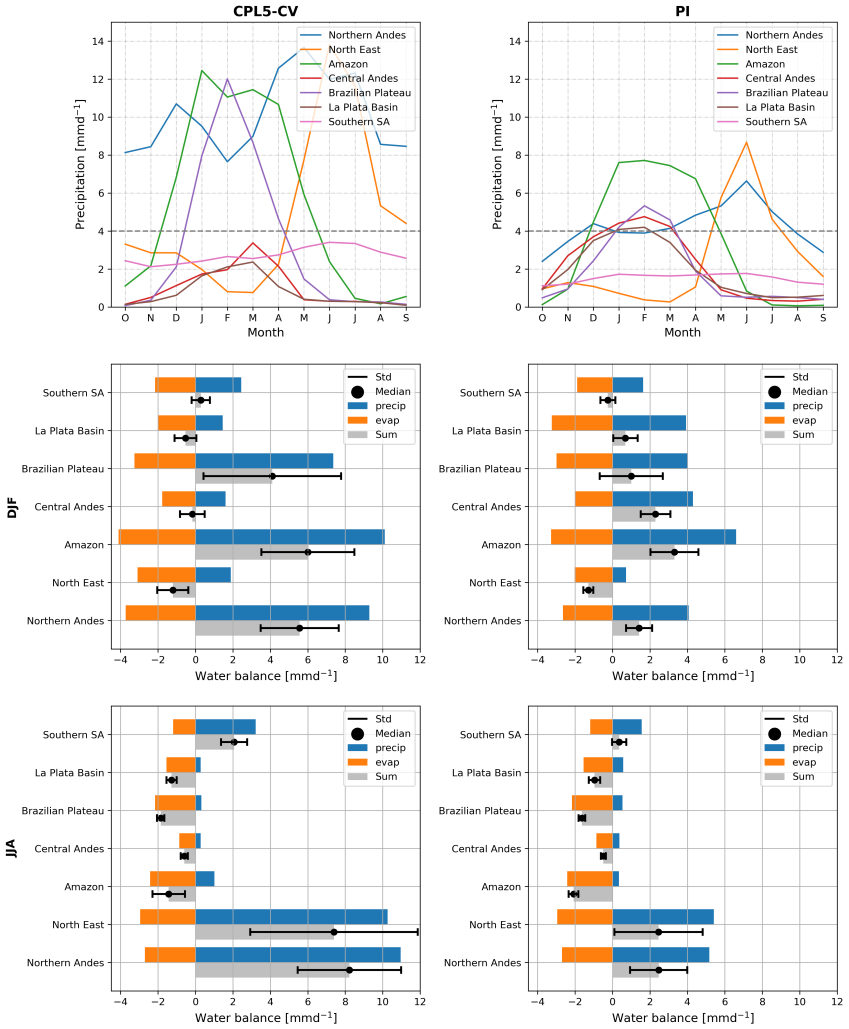

Figure 21: Monthly precipitation (upper row), as well as regional Precipitation – Evaporation (P-E) water budgets for CPL5 (left) and the PI reference simulation (right). Regions correspond to the defined in section 3 and shown in Figure 7.

The Monthly precipitation charts strengthen what could already be observed in Figure 21. The precipitation in low-latitude regions (Northern Andes, north-east South America, Amazon basin and Brazilian Plateau) increases strongly, while subtropical regions such as the La Plata Basin and Central Andes receive less precipitation (cf. Regions defined in section **??** and shown in Figure 7). Further, it is notable that while the precipitation in the respective wet season increases by a factor of ~ 2 or more, the dry seasons are still very pronounced, resembling the pre-industrial dry seasons, which are known to be

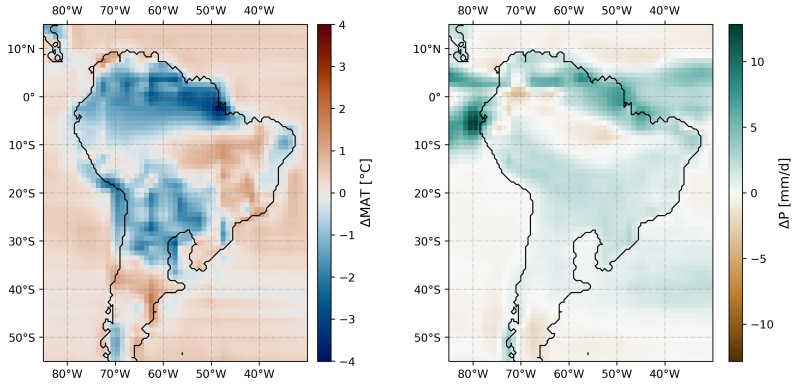

Figure 22: Differences in simulated mean air temperature (left) and mean precipitation (right) between LOR6-CV and CPL5-CV.

dry-biased (cf. Ch.4). Compared to the precipitation, the evaporation trends show less regional variation, increasing evaporation in DJF, and almost no differences during JJA. Therefore, changes in P-E are mostly driven by changes in precipitation.

5.2 The Influence of the Model Version

To investigate the effect of the known model biases on the simulated climate and to be able to constrain their effects on the simulated SAMS and hydrology, I compare CPL5-CV to LOR6-CV, which was performed using the same vegetation map and forced by the SST averaged over the CPL5-CV reference period.
LMDZOR6-CV shows a MAT increase of 8.84 ± 0.03 K for the MMCO, which is almost identical compared to CPL5-CV. For South America, it predicts lower temperatures over northern and central South America, which resemble the correction of the warm bias for the modern period (cf. Ch. 4). Also, it predicts significantly higher precipitation ($\Delta p \approx 5$ mm) for broad parts of South America, apart from the central Amazon and Southern South America (cf Fig. 22, cf. Fig. 23). The seasonal ITCZ position remains very similar to the one modeled in CPL5-CV, but the ITCZ widens (cf. Fig. 32). This is connected to an even more extensive meridional expansion of global wind fields.
As CPL5-CV, LOR6-CV shows all main SAMS components (cf. Fig. 23). The Bolivian High shows a north-westward shift compared to the modern reference simulation (cf. Fig. 12) but is located southeast of the mean position in CPL5-CV. The simulation shares the projected connection of the SACZ with a more southern ITCZ and the shift of the main convective activity overseas on the southern tropical Atlantic. The SALLJ is strengthened by ∼50% compared to CPL5-CV, which is a weaker difference than between the historical simulations of the respective models (cf. Ch.4). Compared to CPL5-CV, LOR6-CV shows a wetter La Plata Basin and Central Andes during DJF, and a substantial increase in seasonal precipitation in north-east South America, the Northern Andes, the Brazilian Plateau, and the Amazon Basin. Further, it shows an increase in seasonal precipitation and dry season precipitation, like in the comparison of the historical simulations (cf. Ch. 4). A more detailed look at the two precipitation types, convective precipitation and large-scale precipitation, reveals some key differences between the hydrology of the

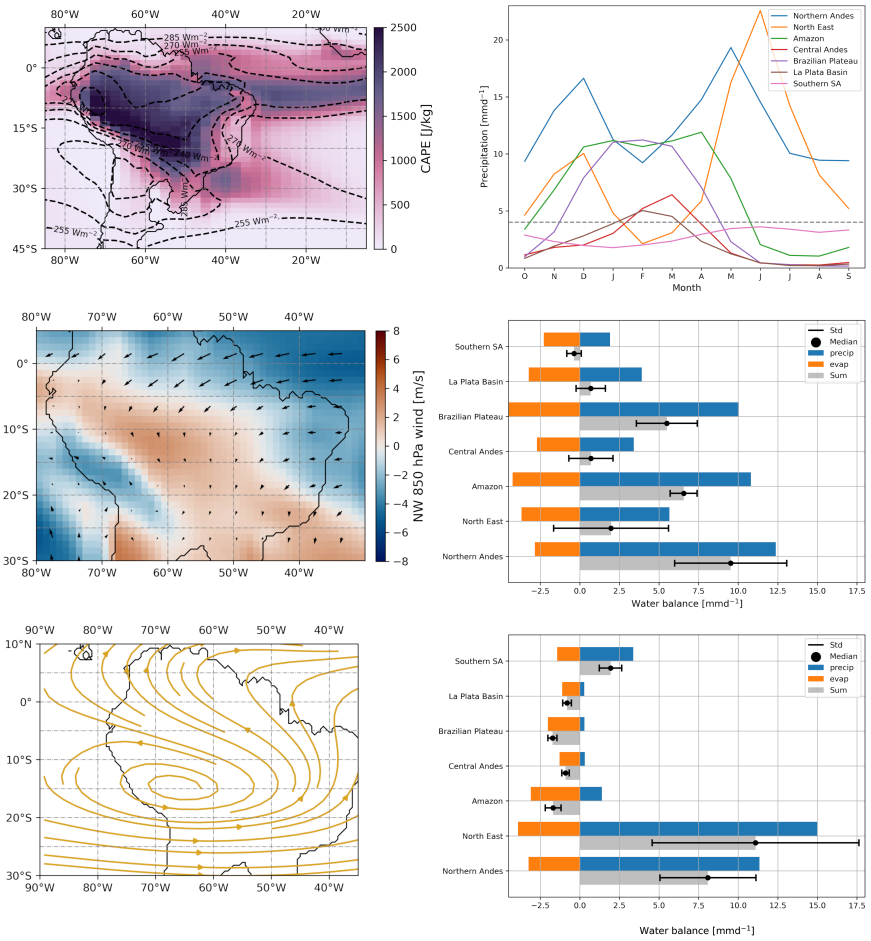

Figure 23: Main SAMS characteristics as simulated in LOR6-CV. Left: DJF averages for SAMS indicators. Top: SACZ as shown by mean CAPE and OLR. Center: Mean wind field and northwesterly wind strength (shading). Bottom: 200 hPa stream plot showing average Bolvian High; Right: Regional hydrology of LOR6-CV. Top: Monthly average precipitation. Center: DJF water budget. Bottom: JJA water budget.

two simulations. Convective precipitation, which makes up 40% of all South-American precipitation in CPL5-CV, strongly increases almost everywhere on the continent. Despite further decreased large-scale precipitation, this leads to wetter subtropics, especially during DJF.
If one compares LMDZOR-CV to the preindustrial control simulation of IPSL-CM6-LR, the MMCO's patterns of hydrological change yield a different picture. The austral winter (JJA) shows significantly increased precipitation in northern South America (NA, NESA) and Southern South America but shows a decrease of precipitation in the Amazon in between 40°S and 5°S. The projected trends for DJF precipitation are similar to CPL5-CV - PI, showing a general increase of precipitation for all regions but the CA and LPB, which become slightly dryer.
An analysis of a few key variables averaged over South America shows plausible mechanisms leading to the different hydrology between the two model types (cf. Fig. 24). For most variables, the results of LOR6-DV and LOR6-CV, and LOR5-DV and CPL5-CV are clustered, showing that the model version makes a greater difference than the vegetation configuration.
During JJA, IPSL-CM5A2 shows a higher westward moisture transport in the tropics and more southward moisture transport between low-to-middle latitudes. During DJF, the LOR6 simulations show a decreased meridional moisture transport south of 25°S and a southward shift of the mid-latitude moisture transport associated with the poleward shift of the westerlies. As for the historical simulations, IPSL-CM6-LR exhibits a higher cloud cover in the low to mid-latitudes during both DJF and JJA (cf. Ch. 4). This results in lower estimates of downwelling short-wave radiation and outgoing long-wave radiation. Incidentally, the convective and large-scale precipitation in the tropics are higher. IPSL-CM6-LR finds a broader meridional distribution in DJF convective precipitation, while differences in JJA precipitation concentrate on the tropics, showing a consistently low precipitation estimate between 30°S and 10°S. A surprising result is the enhanced equatorial large-scale precipitation simulated in LOR5-DV. However, this is not thought to be caused by the simulated vegetation rather than an unresolved increase in moisture advection (cf. Fig. 24).

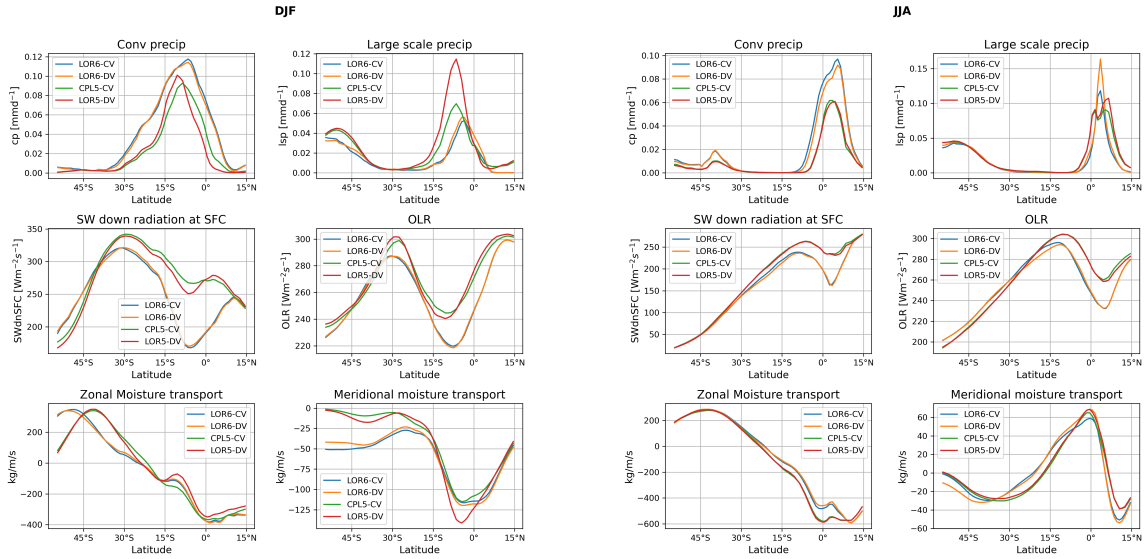

Figure 24: Seasonal zonal means for the simulations CPL5-CV, LOR5-DV, LOR6-CV and LOR6-DV, averaged over South America (80°W-40°W), during DJF (left) and JJA (right). The variables include convective precipitation, large scale precipitation, downwelling short-wave radiation at the surface. outgoing longwave radiation (OLR), the zonal mean moisture transport and meridional mean moisture transport.

5.3 Dynamic Simulations of the Mid-Miocene Vegetation

The analysis of section 5.2 shows that differences in modeled climate caused by differences in parameterization are greater than the differences from dynamic vegetation. The respective dynamic vegetation simulations show no significant difference in the modeled SAMS features compared to their constant vegetation control simulations. Still, dynamic vegetation can affect the local hydrology and be a good indicator of the prevailing climate. Therefore, I compare the modeled PFT distributions of the experiments LOR5-INIT, LOR5-DV, and LOR6-DV. LOR5-DV, which differs from LOR5-INIT in being forced with the equilibrated SSTs, shows a stronger polarity between the tropics and the subtropics in terms of vegetation, like a stronger tropical evergreen forest dominance in the low latitudes and more bare soil (desert/shrubland) in the tropics (cf. Fig. 25). At the Brazilian Plateau and Atlantic coast it shows more tropical forests than the initial dynamical vegetation simulation. LOR6-DV, which is forced by the same SSTs, shows a reduction of the subtropical arid belt and a southward expansion of tropical forests by 10°. Warm-temperate forests dominating SSA up to 30°S, and only a thin band of C3-dominated grassland and a small Atacama desert remains. This produces a misfit with the proxies for grassland around 40°S, as it only portrays grasses up to 33°S.
There are only minor differences between the dynamic vegetation and fixed vegetation experiments of the respective model versions. In general, large-scale precipitation and zonal moisture transport in the tropics are slightly enhanced in the DV experiments (cf. Fig. 24). Another typical pattern in the DV experiments is a negative P-E balance between the tropics and subtropics during JJA (cf. Fig. 26). A further investigation shows

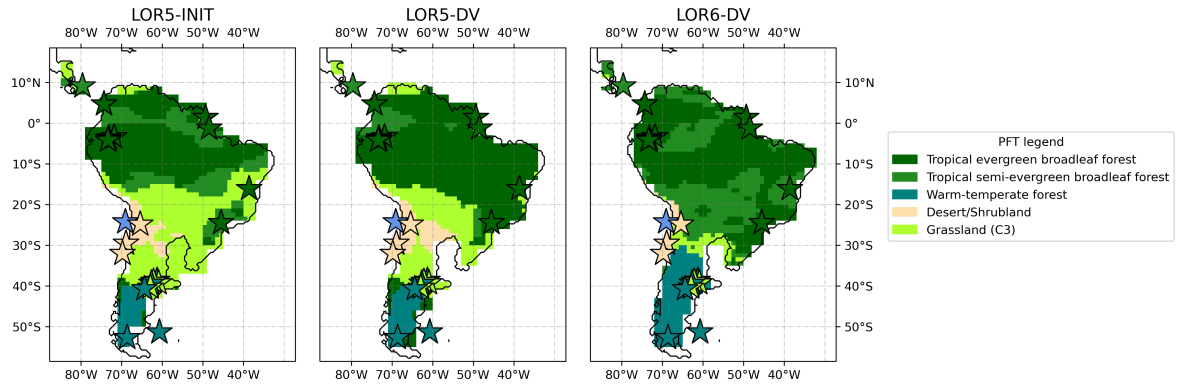

Figure 25: Dominant plant functional type (PFT) for each South American grid point during the MMCO, as modeled by three dynamical vegetation simulations LOR5-INIT, LOR5-DV and LOR6-DV (left to right). The stars indicate proxy locations from Mid-Miocene vegetation proxies Pound et al. (2012), their color indicates the attributed PFT.

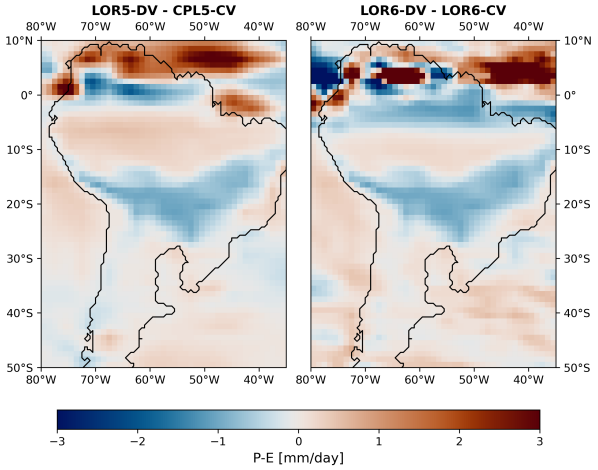

Figure 26: Differences in JJA water balance (P-E) between CPL5-CV and LOR5-DV (left), as well as LOR6-CV and LOR6-DV (right).

that year-round lower soil moisture accompanies the negative P-E caused compared to the CV experiments, which motivates an investigation of the role of soil moisture. The difference in simulated soil moisture between the model versions is extensive and reflects the aridity of IPSL-CM5A2 in the subtropics. LOR6-DV shows 1.5–3 times as high values for soil moisture as LOR6-DV around the year, especially during the dry period (cf. Fig.27).

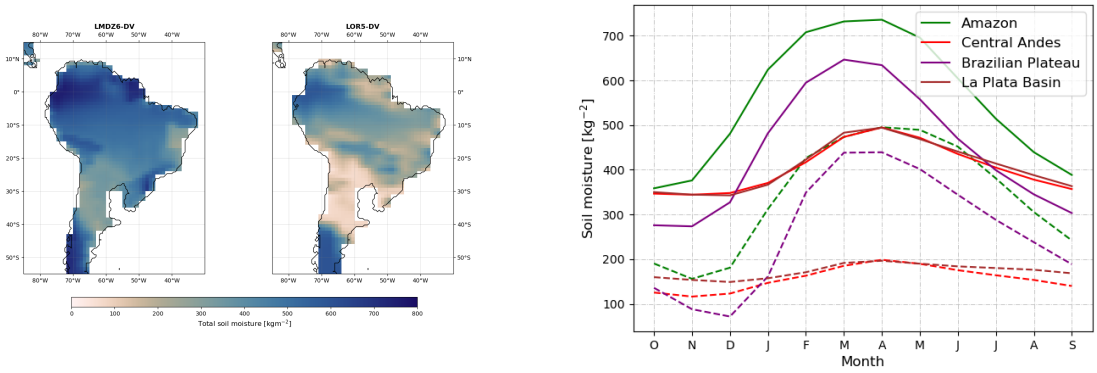

Figure 27: Soil moisture as modeled in LOR6-DV and LOR5-DV. Left: Average spatial distribution. Right: Average yearly cycle (solid lines: LOR6-DV, dashed lines LOR5-DV).

6 Discussion

6.1 Global Temperatures and Ocean Circulation

The estimated warming of 8.73 K (LOR6-DV) 8.85 K (CPL5-CV) compared to the preindustrial lies within the uncertainty of proxy reconstruction (7.6 ± 2.3 K) (Goldner et al. 2014). Like the MioMIP ensemble, CPL5-CV overestimates the meridional SST and MAT gradients (Burls et al. 2021). Figure 28 (left) displays, that most proxies show warmer SSTs at mid-latitudes, and lower SSTs at low-latitudes compared to CPL5-CV. This may be partially explained through IPSL-CM5A2s tuning-induced low SW CRF at mid-latitudes (Sepulchre et al. 2020a), but is likely only part of the truth, as many other models underestimate the MAT in high-latitude regions and overestimate the meridional temperature gradient (Henrot et al. 2017). This bias also affects simulations of other paleoclimatological periods, like the Eocene, and is referred to as the 'equable climate' problem (Huber and Caballero 2011). Another factor for the high estimated SST gradient is the weak meridional overturning circulation, which leads to SST biases in modern-day simulations (Wang et al. 2014) and might lead to an underestimation of the meridional heat transport in the MMCO. As Figure 28 (right) shows, this is also observed in CPL5-CV. The Atlantic branch only shows an AMOC strength of only 5.16 Sv, compared to 10.5 Sv in the PI simulation. This can partially be explained through the open CAS, which shows a 1.69 Sv current from the Pacific to the Atlantic Ocean. The open Tethys gateway accounts for another 1.30 Sv of surface water being transported eastward from the Atlantic. The result resembles the modeling study by Pillot et al. (2022), who found less intense North Atlantic deep water formation and overturning as a result of mid-Miocene paleogeography. This has been previously described by Von Der Heydt and Dijkstra (2008), showing that the heat and salinity exchange at mid-latitudes is responsible for a weakened overturning, and the northern extend of the Atlantic and Pacific Ocean can induce a bifurcation of the overturning circulation. However, very little overturning is observed in the Pacific (0.46 Sv). An increased freshwater influx might explain the weak overturning and its distribution among the basins. However, further investigation into this matter is beyond the scope of this study.

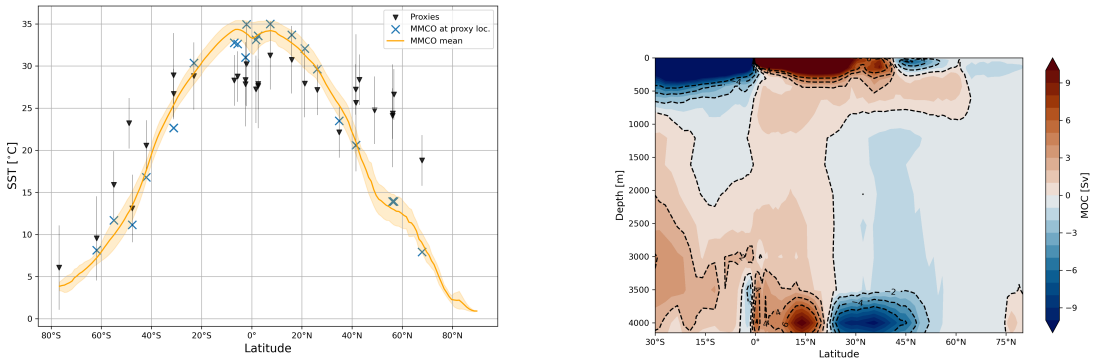

Figure 28: Latitudinal distribution of SST proxies and average model SSTs of CPL5-CV at the corresponding position. The shaded area depicts the zonal standard deviation of SSTs. Markers show the collection of SST proxies for the MMCO presented in Burls et al. (2021) as well as their uncertainty (left). Global Meridional Overturning Circulationin Sv as modeled in CPL5-CV for the MMCO

6.2 Influence of Large-Scale Winds and Pressure

The observed simulated northward expansion of atmospheric cells and wind system is suspected to be caused by the global warming and changed meridional temperature gradient. The position of the subtropical jets has been shown to be mainly determined by the meridional SST gradient (cf. Jiang and Yan 2020). Further, the latitudinal expansion of wind systems is associated with a expansion of the Hadley cell and its associated circulation, which has been previously described for warmer climates, including paleoclimatic periods such as the Pliocene and the MMCO (Lu et al. 2018; Carrapa et al. 2019; Brierley et al. 2009). However, this is associated with a broadening and slight weakening of the easterlies. The Hadley cell is stronger in the LMDZOR6 simulations, probably driven by the intensified convection. A (seasonal) poleward extension of wind systems has been found for the MMCO, without any additional GHG forcing, and attributed to a reduction in the meridional heat gradient solely caused by paleogeography (Herold et al. 2011). The circulation of LOR6-CV and LOR6-DV are taken to be reasonable estimates of the MMCO circulation, CPL5-CV is thought to present too-equatorward subtropical westerlies, and LOR5-DV presents an outlier in terms of its estimate of enhanced tropical easterlies. This poleward expansion can also explain the observed migration of the subtropical highs, and the weakening of the easterlies could explain their respective weakening (Spinks and Lin 2015). A mediating factor on the influence of the changed wind fields on the South American climate is that the continent experienced a northward tectonic drift of about two degrees since the MMCO. Therefore, a relative poleward expansion of two degrees would cancel out on the southern hemispheric part of the continent, while it amplifies to a four-degree difference on the northern hemisphere (assuming an idealized equatorial symmetric circulation and neglecting, that part of the continent changed hemispheres). The MMCO simulations show a reduced orographic blocking due to the lower Andean paleogeography, which increases the lower level zonal flow at low-mid latitudes and weakens the meridional jets toward both sides of the Andes (cf. Fig. 16). This

has been previously shown in sensitivity experiments removing the Andes (Junquas et al. 2016; Sepulchre et al. 2009). These changes change the wind-driven ocean currents and are thought to contribute to the observed SST patterns. For example, the above-average warming at the mid-latitude Pacific coast and reduced warming at the tropical Pacific coast (cf. Fig. 17) is considered to be caused by a northward shift of the Humboldt current, which has previously been found to arise from reduced north wind stress in the East Pacific in reaction to lower Andes (Sepulchre et al. 2009).

6.3 Clouds and convective Processes

Like in the preindustrial, IPSL-CM5A2 and LMDZOR6 exhibit differences in the modeled radiation balance, atmosphere-land interaction, and interaction with orography. The improved cloud physics of IPSL-CM6-LR results in an increased cloud cover in the tropics compared to IPSL-CM5, leading to a decrease of downwelling shortwave radiation and, in particulate, a decreased temperature estimate in the Amazon region. Since the MMCO is much warmer and tropical climates reach higher latitudes, these improvements are considered even more critical in the MMCO than in the PI. As IPSL-CM6 still shows a warm bias in the Amazon region for the PI, and the meridional temperature gradient is overestimated, it suggests that the LMDZOR6 simulations still depict too-warm tropics during the MMCO. Convective processes are significantly increased in the MMCO in both model configurations, but LMDZOR6 shows an approximately four times higher convective available potential energy than CPL5-CV. This throws up the question of whether convection is overestimated in LMDZOR6, as has been reported for parts of the high latitudes (Boucher et al. 2020a). Overall, there is much more evidence for the underestimation of tropical convection in IPSL-CM5A2 due to its tuning (Sepulchre et al. 2020a) and less elaborate parameterization (cf. Ch. 4). Further, the greatly increased vertical resolution and improved parameterization of LMDZ6, as well as the improved atmosphere-land interaction, are considered to result in better convection estimates. Therefore, I consider the broader ITCZ and stronger Hadley cell, strong central South American convection, and increased convective precipitation of LMDZOR6 to reflect MMCO conditions better. The historical analysis shows that the atmosphere-ocean coupled IPSL-CM6-LR is prone to simulate a too-southern ITCZ in eastern South America (cf. Fig. 9), worsening in comparison to IPSL-CM5. However, no significant difference in ITCZ position between CPL5-CV and the LOR6 experiments can be found, potentially because they are forced with CPL5-CVs SSTs. (cf. Fig. 22).

6.4 Characteristics of the dynamic SAMS Features

There are three differences in the appearance of the SACZ that are thought to be caused by different phenomena. All simulations show an intensification of the SACZ with a slightly detached, intense convective area in the southern tropical Atlantic. The fact that the simulated spatial patterns of the SACZ still strongly resemble across different model versions, despite the differences in subtropical westerly extension and convective physics, shows the robustness of this result. Further, the SACZ appears to be slightly tilted zonally. Junquas et al. (2016) find a similar behavior in simulations removing

the Andean topography. This limits the moisture transport to the LPB, depriving it of moisture and energy, and leads to a more eastward formation of the SACZ. The correlation of SALLJ velocities and SACZ position has been shown for observational data as well (Marengo et al. 2004). Therefore, the reduced SALLJ strength due to a lowered Andean topography during the MMCO is thought to contribute to the more northern realization of the SACZ. Secondly, the strength and position of the BH have been shown to influence the position of the SACZ (Van Der Wiel et al. 2015). A BH strengthening through increased Amazonian convection is considered a means to intensify Rossby wave refraction, leading to a more zonal appearance of the SACZ. The dipole structure of the SACZ is considered to arise from a combination of two factors. The decreased transport of warm, moist air to the La Plata Basin makes this region dryer and dynamically more stable, suppressing convection. The fact that this does not extend to the tropical Atlantic is attributed to the strengthening and overproportional warming of the Brazil current, which is considered to cause a strong increase in over-sea convection. The position of the BH differs significantly between IPSL-CM5A2 and LMDZOR6. This is thought to be caused by the different extensions of the mid-latitude upper westerlies. CPL5-CV has previously been discussed to show a too-equatorward extension of the upper-level westerlies, which is thought to cause a more northern position compared to LMDZOR. The relative northwestward shift of the BH from the PI to the MMCO seen in both model configurations is considered to be caused by the respective shift of the main convective activity over the Amazon, as discussed in Lenters and Cook (1997). The fact that both models show a weaker SALLJ is attributed to the lowered Andean orography and thus reduced blocking effect. The fact that LMDZOR6 shows a higher SALLJ strength is considered to be caused by its higher resolution and subscale grid orography scheme. An additional factor to consider is the weakened easterlies, which reduce the strength of the diverted wind during DJF. The northwesterly wind field is considered to give a robust estimate of SALLJ intensity, as this phenomenon manifests in a high frequency during DJF, and a strong vertical wind shear is present in every simulation. However, high-resolution simulations and analysis of sub-daily data, which are necessary to resolve individual SALLJ events, were not performed in this study. Further research into the behavior of the SALLJ at these timescales and at different stages of the Andean uplift could be beneficial to understanding the evolution of the SAMS during the Neogene and beyond.

6.5 Seasonal Hydrology

The simulated onset and duration of the SAMS depend on the used model configuration. IPSL-CM5A2 shows little differences in timing between the MMCO and PI, and it is thought to show a too-intense dry season, like in present-day (cf. Ch. 4). LMDZOR6 shows a later onset of the summer monsoon ($\sim$1.5 months), which is in accordance with the observed later peak in the tropical Atlantic SST gradient, shown to be connected to the timing of the onset (cf. section 5.1, Espinoza et al. 2020). A first-order thermodynamic estimate for precipitation magnitudes of paleoclimates as a reaction to changes in temperature can be done using the Clausius-Claperyon law (Khon et al. 2010). For the global warming of 8.8 K, which is close to the warming estimates for South America, the saturation vapor pressure increasing by $\sim$75%, giving an estimate of the increased

precipitation capacity. The best estimate for the MMCO's hydrology is considered to stem from LOR6-DV, which uses the more elaborate model configuration and includes vegetation feedbacks. It exhibits a ∼50% increase in precipitation in DJF and a ∼10% decrease in JJA. The disproportionately low increase in (austral) summer precipitation and decrease in winter precipitation could be explained through the weakened easterlies and a low increase in eastward moisture transport, combined with the southward shift of the ITCZ. This is consistent with the previous modeling study by Nadoya and Tabor (2022), which found an increase in the winter monsoon precipitation and a weakening of the summer precipitation. Scholz et al. (2020) find an increased seasonality of precipitation in northern Columbia during the MMCO from isotope measurements of mollusks, supporting this observation. However, I cannot confirm the more northern ITCZ hypothesized in the latter study, as my simulation produces this increased seasonality with a more southern ITCZ. This produces an increase in precipitation from the ITCZ during JJA and a decrease between January and March in NESA. The Northern Andes region shows an influence of the ITCZ year-round, with peaks in November and May, similar to the present. The Amazon Basin and the Brazilian Plateau are found to share this increased seasonality, with a substantial increase in DJF precipitation and a slight decrease in JJA precipitation. The paleobotanical proxies in these regions consist exclusively of tropical vegetation (cf. Pound et al. 2012), which is in accordance with the high precipitation. Although the precipitation at the Brazilian Plateau shows a strong seasonality, this suggests that there was enough precipitation during the dry season to support tropical vegetation. The decrease in precipitation in the Central Andes and La Plata Basin are in accordance with the study by Junquas et al. (2016), who performed a sensitivity simulation of the SAMS removing the Andean topography and found a $\sim 50\%$ reduction of LPB and CA precipitation. CPL5-CV finds an even more considerable decrease, taken to be caused by a combination of the decreased topography, SALLJ, and subtropical dry bias caused by too-weak convective precipitation. LMDZOR6 confirms this trend, even though it shows a minor reduction of DJF precipitation in the La Plata Basin. Proxies indicate a drying of the region of the modern Atacama desert related to Andean uplift starting before and continuing during the MMCO (Rech et al. 2006). Considering the discussed SALLJ dynamics, this uplift is expected to have been accompanied by increased moisture in the Central Andes and La Plata Basin.

6.6 Simulated Vegetation

The dynamically simulated biome distributions are considered an effective way to compare the different simulated climates and to incorporate atmosphere-vegetation feedbacks. However, the significant differences in the vegetation schemes between the two model configurations, like calibrations of the PFT albedo and changed soil schemes (Cheruy et al. 2020), add another dimension of variability to the comparison.
Overall, the simulated PFT distributions compare well to the proxies presented by Pound et al. (2012), as all simulations reproduce a fraction of the PFT corresponding to the proxies at the respective location. The larger expansion of tropical and temperate forests and smaller extent of deserts in LOR6-DV agree better with these proxies. However, it doesn't match with the abundant grass proxies at mid-latitudes, which could show an overestimate

of temperate forests. Also, LOR6-DV simulates little boreal vegetation in Antarctica and fewer boreal vegetation in the high-latitude northern hemisphere compared to LOR5-DV, but proxies for these regions are scarce. The decrease in tropical broadleaf evergreen vegetation and rise of deciduous tropical vegetation around the equator in LOR6-DV is likely caused by heat stress and is considered to show that modern PFTs are not sufficient to represent the past tropical vegetation, as previous studies have suggested (Bres et al. 2021). The wet conditions in the East Amazon, exhibited in all simulations, are in accordance with the presence of a tropical, moist Pebas system that existed in the eastern Amazon Basin well before and during the entire MMCO due to geologic subsidence (Jaramillo 2023). The well-documented early Atacama desert (Rech et al. 2006; Jaramillo 2023), is simulated in all dynamical simulations. Compared to the dynamical vegetation study by Henrot et al. (2017), which compares simulated MMCO vegetation from the climate of multiple ESMs, the vegetation distribution by LOR6-DV manages to reproduce the latitudinal expansion of biomes seen in proxies much better. This raises the question of whether this higher latitudinal expansion of vegetation stems mainly from the improved atmosphere model, the improved vegetation scheme, or a combination of both. For the study of (ibid.), part of the answer might be the lower prescribed CO_2 value, but the same difference can be seen in the comparison of LOR6-DV and LMDZOR5. It has been previously shown that while many CMIP5 models show a good approximation of the climatic Koeppen zones, they repeatedly fail to produce the consequent vegetation (Phillips and Bonfils 2015). The differences between LOR5-DV-INIT and LOR5-DV show that the vegetation model is susceptible to changes in vegetation to prescribed SSTs. However, the larger difference between LOR5-DV and LOR6-DV shows that the model configuration plays a more significant role than the prescribed SSTs for this case. Soil moisture has been shown to be a critical factor in why CMIP5 models have trouble reproducing tropical precipitation (Williams et al. 2012), posing a possible land-atmosphere feedback resulting in differences in modeled vegetation. The trend of decreased water budget and soil moisture in the subtropics between DV and CV experiments, which is shared by both model versions, is thought to show increased water usage and transpiration from woody vegetation that was not free to develop in the CV experiments. Soil moisture proves to be significantly enhanced in LOR6-DV and is thought to contribute to the larger extent of woody vegetation through improved growth conditions. As Nieto-Ferreira et al. (2011) demonstrated, the increase of moisture availability, for example, through a reduction of the dry period, is decisive for the spread of woody vegetation. The improved ORCHIDEE parameterizations and added soil layers have proven to significantly reduce the evaporation bias and soil dry bias and lead to a better seasonality in precipitation (Cheruy et al. 2020).

Still, the land surface model has certain limitations that affect the Miocene vegetation. The lack of representation of the Pebas region could have considerable effects on the Eastern Amazon, as the lack of floodplains is considered one of the most significant weaknesses of ORCHIDEE (ibid.). Also, the reduction of tropical broadleaf vegetation at the equator suggests that this specific PFT is not adapted to the hot MMCO climate. Therefore, the addition of tropical PFTs that are better suited to high temperatures and CO_2 levels could benefit the ability to reproduce past Cenozoic climate, as previously suggested by (Boyce and Lee 2017; Bres et al. 2021). Another challenge of this study is the

short reference time of the dynamical vegetation simulations (last 20 years), which enhance the 'noise' of decadal variability and are suspected to mask the low hydrological signals of the vegetation feedbacks. Longer dynamical vegetation simulations could investigate the stability of the simulated vegetation over more extended periods and provide more precise hydrological signals.

6.7 Outlook

The effect of the lower Andean topography, the tectonic shift and the changed ocean circulation on the simulated SAMS are considered significant and seriously complicate a meaningful comparison to future projections which limits adequacy of the MMCO as future analog in terms of the SAMS. There are many teleconnections between local hydrology and large-scale circulations, the most important of which is the El-Nino Southern Oscillation (Cai et al. 2020), which is sensitive to changes in paleotopography (Lu et al. 2018). Additionally, human deforestation and land use play an essential role in the projected South American climate (Staal et al. 2018; Bochow and Boers 2023), and further alienates future climate from paleoclimatological simulations. However, The presented simulations are considered to give a reasonable estimate of the effects a warmer climate can have on the SAMS through a expansion of the Hadley cell and meridional wind systems. The LMDZOR6 experiments show, that atmosphere-land experiment are an efficient way to improve on results of older generation models through the elimimation of biases. Still, the fact, that the SSTs are prescribed, limits the capabilities of the models. The ITCZ position in LMDZOR6 is thought to be inherited from the prescribed IPSL-CM5A2 SSTs, as might other climatological features be. Therefore, an equilibriating simulation using IPSL-CM6-LR is desirable, when it becomes efficient enough. A further limitation of this study in terms of the extent of the validity of the results are the orbital parameters, which were kept constant. The variation of orbital parameters has been shown to affect the position of the ITCZ and thus exert a forcing on the monsoon circulations (Braconnot et al. 2007). Further studies on the sensitivity of the SAMS on orbital changes under high-temperature, low Andes scenarios are needed to project the SAMS's variability during the MMCO.

7 Conclusion

In this study, multiple simulations were performed for the Mid-Miocene Climatic Optimum, comparing the results of different model versions and vegetation configurations. A bias analysis identified the most important sources for biases in simulating the South American climate. The differences in simulated climate in the MMCO show many similarities to the differences in historical simulations. This allows a discussion of the transferal of biases to the MMCO and leads to the conclusion that the atmosphere-land dynamical vegetation simulation LOR6-DV shows the best estimate of MMCO climate out of the performed simulations. The coupled simulation using IPSL-CM5A2 exhibits a too-high meridional temperature gradient like other simulations of warm Cenozoic period but manages to reproduce a high warming, under the high radiative forcing of 840 ppm. The modeled South American Monsoon System shows many trends shared by all simulations, demonstrating the effects of the warmed climate, and changed topography on the SAMS. Generally, the MMCO shows intensified precipitation in reaction to the general warming and enhanced air moisture carrying capacity. The mid-latitude wind and pressure fields shift significantly polewards as a reaction to the warming and changed meridional temperature gradient. This is accompanied by a broadening of the Hadley circulation and weakening of tropical easterly winds, mitigating the general precipitation increase, which is especially strong in the tropical convergence zones. Convection and precipitation over the Amazon and Eastern South America are increased, strengthening the Bolivian High and the South American Convergence cell. However, both features move northward in reaction to a weakened SALLJ and moisture transport to southeast South America, leading to a stagnation to decrease in precipitation in the Central Andes and La Plata Basin. This regional change was identified to be caused by the lower Andean Cordillera in the Mid-Miocene, whose reduced orographic forcing weakens the low-level jets on both sides of the Andes and shows enhanced cross-continental westerlies during JJA, contributing to an intensified dry season between 5°S and 40°S. LMDZOR6 shows a larger meridional expansion of tropical and temperate biomes due to its reduced subtropical dry bias and improved vegetation model. Atmosphere-vegetation feedbacks investigated through fixed vegetation control simulations are found to be small against differences in the model version. LMDZOR6 outperforms previous simulations with older model generations in reproducing the higher extent of tropical and temperate forests during the MMCO. Thus, simulations put forward in this study contribute to the collection of experiments performed in the effort to understand mid-Miocene warmth. Further, the detailed analysis of the dynamical changes in the simulations compared to present-day adds to the understanding of the evolution of the South American Monsoon System in the Cenozoic.

References

Anderson, J. B. et al. (2011). "Progressive Cenozoic Cooling and the Demise of Antarctica's Last Refugium". In: *Proceedings of the National Academy of Sciences* 108.28, pp. 11356–11360. DOI: 10.1073/pnas.1014885108.

Bochow, N. and N. Boers (2023). "The South American monsoon approaches a critical transition in response to deforestation". en. In: *Science Advances* 9.40, eadd9973. DOI: 10.1126/sciadv.add9973.

Boucher, O. et al. (2020a). "Presentation and Evaluation of the IPSL-CM6A-LR Climate Model". In: *Journal of Advances in Modeling Earth Systems* 12.7. DOI: 10.1029/2019MS002010.

— (2020b). "Presentation and Evaluation of the IPSL-CM6A-LR Climate Model". en. In: *Journal of Advances in Modeling Earth Systems* 12.7. DOI: 10.1029/2019MS002010.

Boyce, C. K. and J.-E. Lee (2017). "Plant Evolution and Climate Over Geological Timescales". en. In: *Annual Review of Earth and Planetary Sciences* 45.1, pp. 61–87. DOI: 10.1146/annurev-earth-063016-015629.

Braconnot, P. et al. (1999). "Synergistic Feedbacks from Ocean and Vegetation on the African Monsoon Response to Mid-Holocene Insolation". In: *Geophysical Research Letters* 26.16, pp. 2481–2484. DOI: 10.1029/1999GL006047.

Braconnot, P. et al. (2007). "Results of PMIP2 Coupled Simulations of the Mid-Holocene and Last Glacial Maximum – Part 2: Feedbacks with Emphasis on the Location of the ITCZ and Mid- and High Latitudes Heat Budget". In: *Climate of the Past* 3.2, pp. 279–296. DOI: 10.5194/cp-3-279-2007.

Bres, J. et al. (2021). "The Cretaceous Physiological Adaptation of Angiosperms to a Declining <I>P</I>CO₂: A Modeling Approach Emulating Paleo-Traits". In: *Biogeosciences* 18.20, pp. 5729–5750. DOI: 10.5194/bg-18-5729-2021.

Brierley, C. M. et al. (2009). "Greatly Expanded Tropical Warm Pool and Weakened Hadley Circulation in the Early Pliocene". en. In: *Science* 323.5922, pp. 1714–1718. DOI: 10.1126/science.1167625.

Bruch, A. A., T. Utescher, and V. Mosbrugger (2011). "Precipitation Patterns in the Miocene of Central Europe and the Development of Continentality". In: *Palaeogeography, Palaeoclimatology, Palaeoecology* 304.3-4, pp. 202–211. DOI: 10.1016/j.palaeo.2010.10.002.

Burls, N. J. et al. (2021). "Simulating Miocene Warmth: Insights From an Opportunistic Multi-Model Ensemble (MioMIP1)". In: *Paleoceanography and Paleoclimatology* 36.5. DOI: 10.1029/2020PA004054.

Cai, W. et al. (2020). "Climate impacts of the El Niño–Southern Oscillation on South America". en. In: *Nature Reviews Earth & Environment* 1.4, pp. 215–231. DOI: 10.1038/s43017-020-0040-3.

Carrapa, B., M. Clementz, and R. Feng (2019). "Ecological and hydroclimate responses to strengthening of the Hadley circulation in South America during the Late Miocene cooling". en. In: *Proceedings of the National Academy of Sciences* 116.20, pp. 9747–9752. DOI: 10.1073/pnas.1810721116.

Carvalho, L. M. V., C. Jones, and B. Liebmann (2004). "The South Atlantic Convergence Zone: Intensity, Form, Persistence, and Relationships with Intraseasonal to Interannual Activity and Extreme Rainfall". In: *Journal of Climate* 17.1, pp. 88–108. DOI: 10.1175/1520-0442(2004)017<0088:TSACZI>2.0.CO;2.

Cheruy, F. et al. (2020). "Improved Near-Surface Continental Climate in IPSL-CM6A-LR by Combined Evolutions of Atmospheric and Land Surface Physics". In: *Journal of Advances in Modeling Earth Systems* 12.10. DOI: 10.1029/2019MS002005.

Córdova, M., R. Célleri, and A. Van Delden (2022). "Dynamics of Precipitation Anomalies in Tropical South America". In: *Atmosphere* 13.6, p. 972. DOI: 10.3390/atmos13060972.

Correa, I. C., P. A. Arias, and M. Rojas (2021). "Evaluation of Multiple Indices of the South American Monsoon". In: *International Journal of Climatology* 41.S1. DOI: 10.1002/joc.6880.

Da Silva, A. E. and L. M. V. De Carvalho (2007). "Large-Scale Index for South America Monsoon (LISAM)". In: *Atmospheric Science Letters* 8.2, pp. 51–57. DOI: 10.1002/asl.150.

De Carvalho, L. M. V. and I. F. A. Cavalcanti (2016). "The South American Monsoon System (SAMS)". In: *The Monsoons and Climate Change*. Ed. by L. M. V. De Carvalho and C. Jones. Cham: Springer International Publishing, pp. 121–148. DOI: 10.1007/978-3-319-21650-8_6.

De Rosnay, P. et al. (2002). "Impact of a Physically Based Soil Water Flow and Soil-Plant Interaction Representation for Modeling Large-Scale Land Surface Processes: PHYSICALLY BASED SOIL HYDROLOGY IN GCM". In: *Journal of Geophysical Research: Atmospheres* 107.D11, ACL 3-1-ACL 3–19. DOI: 10.1029/2001JD000634.

De Vleeschouwer, D. et al. (2017). "Alternating Southern and Northern Hemisphere Climate Response to Astronomical Forcing during the Past 35 m.y." In: *Geology* 45.4, pp. 375–378. DOI: 10.1130/G38663.1.

Dutton, J. F., C. J. Poulsen, and J. L. Evans (2000). "The Effect of Global Climate Change on the Regions of Tropical Convection in CSM1". In: *Geophysical Research Letters* 27.19, pp. 3049–3052. DOI: 10.1029/2000GL011542.

Elbaum, E. et al. (2022). "Uncertainty in Projected Changes in Precipitation Minus Evaporation: Dominant Role of Dynamic Circulation Changes and Weak Role for Thermodynamic Changes". In: *Geophysical Research Letters* 49.12, e2022GL097725. DOI: 10.1029/2022GL097725.

Espinoza, J. C. et al. (2014). "The Extreme 2014 Flood in South-Western Amazon Basin: The Role of Tropical-Subtropical South Atlantic SST Gradient". In: *Environmental Research Letters* 9.12, p. 124007. DOI: 10.1088/1748-9326/9/12/124007.

Espinoza, J. C. et al. (2020). "Hydroclimate of the Andes Part I: Main Climatic Features". In: *Frontiers in Earth Science* 8, p. 64. DOI: 10.3389/feart.2020.00064.

Fan, X. et al. (2020). "Global Surface Air Temperatures in CMIP6: Historical Performance and Future Changes". In: *Environmental Research Letters* 15.10, p. 104056. DOI: 10.1088/1748-9326/abb051.

Figueroa, S. N., P. Satyamurty, and P. L. Da Silva Dias (1995). "Simulations of the Summer Circulation over the South American Region with an Eta Coordinate Model". In: *Journal of the Atmospheric Sciences* 52.10, pp. 1573–1584. DOI: 10.1175/1520-0469(1995)052<1573:SOTSCO>2.0.CO;2.

Fretwell, P. et al. (2013). "Bedmap2: Improved Ice Bed, Surface and Thickness Datasets for Antarctica". In: *The Cryosphere* 7.1, pp. 375–393. DOI: 10.5194/tc-7-375-2013.

Frigola, A., M. Prange, and M. Schulz (2018). "Boundary Conditions for the Middle Miocene Climate Transition (MMCT v1.0)". In: *Geoscientific Model Development* 11.4, pp. 1607–1626. DOI: 10.5194/gmd-11-1607-2018.

Gadgil, S. (2018). "The Monsoon System: Land–Sea Breeze or the ITCZ?" In: *Journal of Earth System Science* 127.1, p. 1. DOI: 10.1007/s12040-017-0916-x.

Gan, M. A., V. B. Rao, and M. C. L. Moscati (2005). "South American Monsoon Indices". In: *Atmospheric Science Letters* 6.4, pp. 219–223. DOI: 10.1002/asl.119.

Garreaud, R. D. et al. (2009). "Present-day South American climate". en. In: *Palaeogeography, Palaeoclimatology, Palaeoecology* 281.3-4, pp. 180–195. DOI: 10.1016/j.palaeo.2007.10.032.

Gasson, E. et al. (2016). "Dynamic Antarctic Ice Sheet during the Early to Mid-Miocene". In: *Proceedings of the National Academy of Sciences* 113.13, pp. 3459–3464. DOI: 10.1073/pnas.1516130113.

Geen, R. et al. (2020). "Monsoons, ITCZs, and the Concept of the Global Monsoon". In: *Reviews of Geophysics* 58.4, e2020RG000700. DOI: 10.1029/2020RG000700.

Giannini, A., R. Saravanan, and P. Chang (2004). "The Preconditioning Role of Tropical Atlantic Variability in the Development of the ENSO Teleconnection: Implications for the Prediction of Nordeste Rainfall". In: *Climate Dynamics* 22.8, pp. 839–855. DOI: 10.1007/s00382-004-0420-2.

Goldner, A., N. Herold, and M. Huber (2014). "The Challenge of Simulating the Warmth of the Mid-Miocene Climatic Optimum in CESM1". In: *Climate of the Past* 10.2, pp. 523–536. DOI: 10.5194/cp-10-523-2014.

Groeneveld, J. et al. (2014). "Glacial Induced Closure of the Panamanian Gateway during Marine Isotope Stages (MIS) 95–100 (2.5 Ma)". In: *Earth and Planetary Science Letters* 404, pp. 296–306. DOI: 10.1016/j.epsl.2014.08.007.

Gulizia, C. and I. Camilloni (2015). "Comparative Analysis of the Ability of a Set of CMIP3 and CMIP5 Global Climate Models to Represent Precipitation in South America: COMPARATIVE ANALYSIS OF THE ABILITY OF A SET OF CMIP3 AND CMIP5 MODELS". In: *International Journal of Climatology* 35.4, pp. 583–595. DOI: 10.1002/joc.4005.

Halley, E. (1686). "An Historical Account of the Trade Winds, and Monsoons, Observable in the Seas between and near the Tropicks, with an Attempt to Assign the Physical Cause of the Said Winds". In: *Philosophical Transactions of the Royal Society of London* 16.183, pp. 153–168. DOI: 10.1098/rstl.1686.0026.

Henrot, A.-J. et al. (2017). "Middle Miocene Climate and Vegetation Models and Their Validation with Proxy Data". In: *Palaeogeography, Palaeoclimatology, Palaeoecology* 467, pp. 95–119. DOI: 10.1016/j.palaeo.2016.05.026.

Herold, N., M. Huber, and R. D. Müller (2011). "Modeling the Miocene Climatic Optimum. Part I: Land and Atmosphere*". In: *Journal of Climate* 24.24, pp. 6353–6372. DOI: 10.1175/2011JCLI4035.1.

Holbourn, A. et al. (2010). "Does Antarctic Glaciation Force Migration of the Tropical Rain Belt?" In: *Geology* 38.9, pp. 783–786. DOI: 10.1130/G31043.1.

Huber, M. and R. Caballero (2011). "The early Eocene equable climate problem revisited". en. In: *Climate of the Past* 7.2, pp. 603–633. DOI: 10.5194/cp-7-603-2011.

Jaramillo, C. (2023). "The Evolution of Extant South American Tropical Biomes". In: *New Phytologist*, nph.18931. DOI: 10.1111/nph.18931.

Jaramillo, C. and A. Cárdenas (2013). "Global Warming and Neotropical Rainforests: A Historical Perspective". In: *Annual Review of Earth and Planetary Sciences* 41.1, pp. 741–766. DOI: 10.1146/annurev-earth-042711-105403.

Jiang, N. and Q. Yan (2020). "Evolution of the meridional shift of the subtropical and subpolar westerly jet over the Southern Hemisphere during the past 21,000 years". en. In: *Quaternary Science Reviews* 246, p. 106544. DOI: 10.1016/j.quascirev.2020.106544.

Junquas, C. et al. (2016). "Influence of South America Orography on Summertime Precipitation in Southeastern South America". In: *Climate Dynamics* 46.11-12, pp. 3941–3963. DOI: 10.1007/s00382-015-2814-8.

Khon, V. C. et al. (2010). "Response of the hydrological cycle to orbital and greenhouse gas forcing". en. In: *Geophysical Research Letters* 37.19, 2010GL044377. DOI: 10.1029/2010GL044377.

Kothawale, D. R. and K. R. Kumar (2002). "Tropospheric Temperature Variation over India and Links with the Indian Summer Monsoon : 1971-2000". In: *MAUSAM* 53.3, pp. 289–308. DOI: 10.54302/mausam.v53i3.1646.

Krinner, G. et al. (2005). "A Dynamic Global Vegetation Model for Studies of the Coupled Atmosphere-Biosphere System: DVGM FOR COUPLED CLIMATE STUDIES". In: *Global Biogeochemical Cycles* 19.1. DOI: 10.1029/2003GB002199.

Kuhnt, W. et al. (2004). "Neogene History of the Indonesian Throughflow". In: *Geophysical Monograph Series*. Ed. by P. Clift et al. Vol. 149. Washington, D. C.: American Geophysical Union, pp. 299–320. DOI: 10.1029/149GM16.

Langebroek, P. M., A. Paul, and M. Schulz (2009). "Antarctic Ice-Sheet Response to Atmospheric CO₂ and Insolation in the Middle Miocene". In: *Climate of the Past* 5.4, pp. 633–646. DOI: 10.5194/cp-5-633-2009.

Lenters, J. D. and K. H. Cook (1997). "On the Origin of the Bolivian High and Related Circulation Features of the South American Climate". en. In: *Journal of the Atmospheric Sciences* 54.5, pp. 656–678. DOI: 10.1175/1520-0469(1997)054<0656:OTOOTB>2.0.CO;2.

Lewis, A. R. et al. (2008). "Mid-Miocene Cooling and the Extinction of Tundra in Continental Antarctica". In: *Proceedings of the National Academy of Sciences* 105.31, pp. 10676–10680. DOI: 10.1073/pnas.0802501105.

Li, G. and S.-P. Xie (2014). "Tropical Biases in CMIP5 Multimodel Ensemble: The Excessive Equatorial Pacific Cold Tongue and Double ITCZ Problems*". In: *Journal of Climate* 27.4, pp. 1765–1780. DOI: 10.1175/JCLI-D-13-00337.1.

Liebmann, B. and C. R. Mechoso (2011). "The South American Monsoon System". In: *The Global Monsoon System*. Vol. Volume 5. World Scientific Series on Asia-Pacific Weather and Climate Volume 5. WORLD SCIENTIFIC, pp. 137–157. DOI: 10.1142/9789814343411_0009.

Liebmann, B. et al. (2004). "Subseasonal Variations of Rainfall in South America in the Vicinity of the Low-Level Jet East of the Andes and Comparison to Those in the

South Atlantic Convergence Zone". en. In: *Journal of Climate* 17.19, pp. 3829–3842. DOI: 10.1175/1520-0442(2004)017<3829:SVORIS>2.0.CO;2.

Liebrand, D. et al. (2017). "Evolution of the Early Antarctic Ice Ages". In: *Proceedings of the National Academy of Sciences* 114.15, pp. 3867–3872. DOI: 10.1073/pnas.1615440114.

Lu, Z. et al. (2018). "A Review of Paleo El Niño-Southern Oscillation". en. In: *Atmosphere* 9.4, p. 130. DOI: 10.3390/atmos9040130.

Marengo, J. A. et al. (2004). "Climatology of the Low-Level Jet East of the Andes as Derived from the NCEP–NCAR Reanalyses: Characteristics and Temporal Variability". In: *Journal of Climate* 17.12, pp. 2261–2280. DOI: 10.1175/1520-0442(2004)017<2261:COTLJE>2.0.CO;2.

Marengo, J. A. et al. (2012). "Development of Regional Future Climate Change Scenarios in South America Using the Eta CPTEC/HadCM3 Climate Change Projections: Climatology and Regional Analyses for the Amazon, São Francisco and the Paraná River Basins". In: *Climate Dynamics* 38.9-10, pp. 1829–1848. DOI: 10.1007/s00382-011-1155-5.

Mueller, B. and S. I. Seneviratne (2014). "Systematic Land Climate and Evapotranspiration Biases in CMIP5 Simulations". In: *Geophysical Research Letters* 41.1, pp. 128–134. DOI: 10.1002/2013GL058055.

Nadoya, H. N. and C. R. Tabor (2022). "Investigation of the South American Monsoon during the Miocene Climate Optimum". In: 2022, PP42D–1143.

Nieto-Ferreira, R., T. M. Rickenbach, and E. A. Wright (2011). "The role of cold fronts in the onset of the monsoon season in the South Atlantic convergence zone". en. In: *Quarterly Journal of the Royal Meteorological Society* 137.657, pp. 908–922. DOI: 10.1002/qj.810.

Nobre, C. A. and L. D. S. Borma (2009). "'Tipping points' for the Amazon forest". en. In: *Current Opinion in Environmental Sustainability* 1.1, pp. 28–36. DOI: 10.1016/j.cosust.2009.07.003.

Nogueira, M. (2020). "Inter-Comparison of ERA-5, ERA-interim and GPCP Rainfall over the Last 40 Years: Process-based Analysis of Systematic and Random Differences". In: *Journal of Hydrology* 583, p. 124632. DOI: 10.1016/j.jhydrol.2020.124632.

Oerlemans, J. (2004). "Correcting the Cenozoic δ18O Deep-Sea Temperature Record for Antarctic Ice Volume". In: *Palaeogeography, Palaeoclimatology, Palaeoecology* 208.3-4, pp. 195–205. DOI: 10.1016/j.palaeo.2004.03.004.

Pekar, S. F. and R. M. DeConto (2006). "High-Resolution Ice-Volume Estimates for the Early Miocene: Evidence for a Dynamic Ice Sheet in Antarctica". In: *Palaeogeography, Palaeoclimatology, Palaeoecology* 231.1-2, pp. 101–109. DOI: 10.1016/j.palaeo.2005.07.027.

Phillips, T. J. and C. J. W. Bonfils (2015). "Köppen Bioclimatic Evaluation of CMIP Historical Climate Simulations". In: *Environmental Research Letters* 10.6, p. 064005. DOI: 10.1088/1748-9326/10/6/064005.

Pillot, Q. et al. (2022). "Evolution of Ocean Circulation in the North Atlantic Ocean During the Miocene: Impact of the Greenland Ice Sheet and the Eastern Tethys Seaway". In: *Paleoceanography and Paleoclimatology* 37.8, e2022PA004415. DOI: 10.1029/2022PA004415.

Potter, P. E. and P. Szatmari (2009). "Global Miocene Tectonics and the Modern World". In: *Earth-Science Reviews* 96.4, pp. 279–295. DOI: 10.1016/j.earscirev.2009.07.003.

Pound, M. J. et al. (2012). "Global Vegetation Dynamics and Latitudinal Temperature Gradients during the Mid to Late Miocene (15.97–5.33Ma)". In: *Earth-Science Reviews* 112.1-2, pp. 1–22. DOI: 10.1016/j.earscirev.2012.02.005.

Rae, J. W. et al. (2021). "Atmospheric CO $_2$ over the Past 66 Million Years from Marine Archives". en. In: *Annual Review of Earth and Planetary Sciences* 49.1, pp. 609–641. DOI: 10.1146/annurev-earth-082420-063026.

Rech, J. A. et al. (2006). "Neogene climate change and uplift in the Atacama Desert, Chile". en. In: *Geology* 34.9, p. 761. DOI: 10.1130/G22444.1.

Ring, S. J., S. G. Mutz, and T. A. Ehlers (2022). "Cenozoic Proxy Constraints on Earth System Sensitivity to Greenhouse Gases". In: *Paleoceanography and Paleoclimatology* 37.12, e2021PA004364. DOI: 10.1029/2021PA004364.

Rodwell, M. J. and B. J. Hoskins (2001). "Subtropical Anticyclones and Summer Monsoons". In: *Journal of Climate* 14.15, pp. 3192–3211. DOI: 10.1175/1520-0442(2001)014<3192:SAASM>2.0.CO;2.

Rosa, E. B. et al. (2020). "Automated Detection Algorithm for SACZ, Oceanic SACZ, and Their Climatological Features". In: *Frontiers in Environmental Science* 8, p. 18. DOI: 10.3389/fenvs.2020.00018.

Salazar-Jaramillo, S. et al. (2022). "Changes in Rainfall Seasonality Inferred from Weathering and Pedogenic Trends in Mid-Miocene Paleosols of La Tatacoa, Colombia". In: *Global and Planetary Change* 208, p. 103711. DOI: 10.1016/j.gloplacha.2021.103711.

Sangiorgi, F. et al. (2018). "Southern Ocean Warming and Wilkes Land Ice Sheet Retreat during the Mid-Miocene". In: *Nature Communications* 9.1, p. 317. DOI: 10.1038/s41467-017-02609-7.

Scholz, S. R. et al. (2020). "Isotope Sclerochronology Indicates Enhanced Seasonal Precipitation in Northern South America (Colombia) during the Mid-Miocene Climatic Optimum". In: *Geology* 48.7, pp. 668–672. DOI: 10.1130/G47235.1.

Segura, H. et al. (2020). "Recent changes in the precipitation-driving processes over the southern tropical Andes/western Amazon". en. In: *Climate Dynamics* 54.5-6, pp. 2613–2631. DOI: 10.1007/s00382-020-05132-6.

Sepulchre, P. et al. (2009). "Impacts of Andean uplift on the Humboldt Current system: A climate model sensitivity study". en. In: *Paleoceanography* 24.4, 2008PA001668. DOI: 10.1029/2008PA001668.

Sepulchre, P. et al. (2020a). "IPSL-CM5A2 – an Earth System Model Designed for Multi-Millennial Climate Simulations". In: *Geoscientific Model Development* 13.7, pp. 3011–3053. DOI: 10.5194/gmd-13-3011-2020.

— (2020b). "IPSL-CM5A2 – an Earth system model designed for multi-millennial climate simulations". en. In: *Geoscientific Model Development* 13.7, pp. 3011–3053. DOI: 10.5194/gmd-13-3011-2020.

Silva, G. A. M. and T. Ambrizzi (2006). "Inter-El Niño Variability and Its Impact on the South American Low-Level Jet East of the Andes during Austral Summer Two Case

Studies". In: *Advances in Geosciences* 6, pp. 283–287. DOI: 10.5194/adgeo-6-283-2006.

Simpson, G. C. (1921). "The South-West Monsoon: THE SOUTH-WEST MONSOON". In: *Quarterly Journal of the Royal Meteorological Society* 47.199, pp. 151–171. DOI: 10.1002/qj.49704719901.

Sosdian, S. et al. (2018). "Constraining the Evolution of Neogene Ocean Carbonate Chemistry Using the Boron Isotope pH Proxy". In: *Earth and Planetary Science Letters* 498, pp. 362–376. DOI: 10.1016/j.epsl.2018.06.017.

Spicer, R. A. (2017). "Tibet, the Himalaya, Asian Monsoons and Biodiversity – In What Ways Are They Related?" In: *Plant Diversity* 39.5, pp. 233–244. DOI: 10.1016/j.pld.2017.09.001.

Spinks, J. and Y.-L. Lin (2015). "Variability of the subtropical highs, African easterly jet and easterly wave intensities over North Africa and Arabian Peninsula in late summer: SUBTROPICAL HIGH, AEJ AND AEW VARIABILITY". en. In: *International Journal of Climatology* 35.12, pp. 3540–3555. DOI: 10.1002/joc.4226.

Staal, A. et al. (2018). "Forest-Rainfall Cascades Buffer against Drought across the Amazon". In: *Nature Climate Change* 8.6, pp. 539–543. DOI: 10.1038/s41558-018-0177-y.

Steinthorsdottir, M., P. E. Jardine, and W. C. Rember (2021a). "Near-Future pCO_2 During the Hot Miocene Climatic Optimum". In: *Paleoceanography and Paleoclimatology* 36.1. DOI: 10.1029/2020PA003900.

Steinthorsdottir, M. et al. (2021b). "The Miocene: The Future of the Past". In: *Paleoceanography and Paleoclimatology* 36.4. DOI: 10.1029/2020PA004037.

Stoll, H. M. et al. (2019). "Upregulation of Phytoplankton Carbon Concentrating Mechanisms during Low CO2 Glacial Periods and Implications for the Phytoplankton pCO2 Proxy". In: *Quaternary Science Reviews* 208, pp. 1–20. DOI: 10.1016/j.quascirev.2019.01.012.

Stouffer, R. J. et al. (2017). "CMIP5 Scientific Gaps and Recommendations for CMIP6". In: *Bulletin of the American Meteorological Society* 98.1, pp. 95–105. DOI: 10.1175/BAMS-D-15-00013.1.

Trayler, R. B. et al. (2020). "Patagonian Aridification at the Onset of the Mid-Miocene Climatic Optimum". In: *Paleoceanography and Paleoclimatology* 35.9. DOI: 10.1029/2020PA003956.

Van Der Wiel, K. et al. (2015). "A Dynamical Framework for the Origin of the Diagonal South Pacific and South Atlantic Convergence Zones". In: *Quarterly Journal of the Royal Meteorological Society* 141.691, pp. 1997–2010. DOI: 10.1002/qj.2508.

Vera, C. et al. (2006a). "Toward a Unified View of the American Monsoon Systems". In: *Journal of Climate* 19.20, pp. 4977–5000. DOI: 10.1175/JCLI3896.1.

Vera, C. et al. (2006b). "Climate change scenarios for seasonal precipitation in South America from IPCC-AR4 models". en. In: *Geophysical Research Letters* 33.13, p. L13707. DOI: 10.1029/2006GL025759.

Von Der Heydt, A. and H. A. Dijkstra (2008). "The Effect of Gateways on Ocean Circulation Patterns in the Cenozoic". In: *Global and Planetary Change* 62.1-2, pp. 132–146. DOI: 10.1016/j.gloplacha.2007.11.006.

Wang, C. et al. (2014). "A Global Perspective on CMIP5 Climate Model Biases". In: *Nature Climate Change* 4.3, pp. 201–205. DOI: 10.1038/nclimate2118.

Westerhold, T. et al. (2020). "An Astronomically Dated Record of Earth's Climate and Its Predictability over the Last 66 Million Years". In: *Science* 369.6509, pp. 1383–1387. DOI: 10.1126/science.aba6853.

Williams, C. J. R., R. P. Allan, and D. R. Kniveton (2012). "Diagnosing atmosphere–land feedbacks in CMIP5 climate models". In: *Environmental Research Letters* 7.4, p. 044003. DOI: 10.1088/1748-9326/7/4/044003.

Yin, L. et al. (2013). "How Well Can CMIP5 Simulate Precipitation and Its Controlling Processes over Tropical South America?" In: *Climate Dynamics* 41.11-12, pp. 3127–3143. DOI: 10.1007/s00382-012-1582-y.

Zemp, D. C. et al. (2014). "On the Importance of Cascading Moisture Recycling in South America". In: *Atmospheric Chemistry and Physics* 14.23, pp. 13337–13359. DOI: 10.5194/acp-14-13337-2014.

Zhang, K., W. J. Randel, and R. Fu (2017). "Relationships between Outgoing Longwave Radiation and Diabatic Heating in Reanalyses". In: *Climate Dynamics* 49.7-8, pp. 2911–2929. DOI: 10.1007/s00382-016-3501-0.

Zhang, Q. et al. (2023). "Understanding Models' Global Sea Surface Temperature Bias in Mean State: From CMIP5 to CMIP6". In: *Geophysical Research Letters* 50.4, e2022GL100888. DOI: 10.1029/2022GL100888.

A Appendix

A.1 Supplementary Figures on CPL5-CV

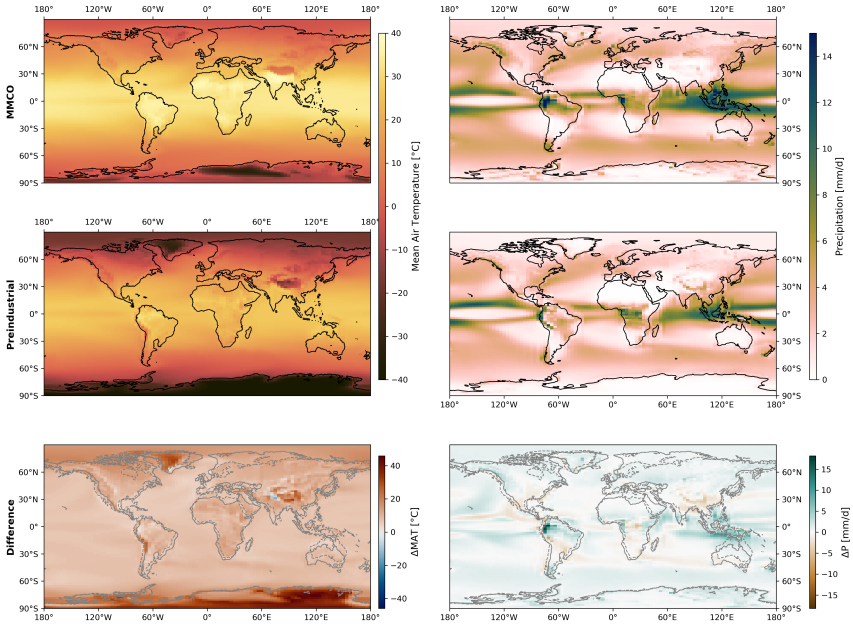

Figure 29: Absolute mean air temparature and mean precipitation fields for CPL5-CV (top) and its preindustrail IPSL-CM5A2 reference simulation (center), as well as their anomaly (CPL5-CV minus PI; bottom).

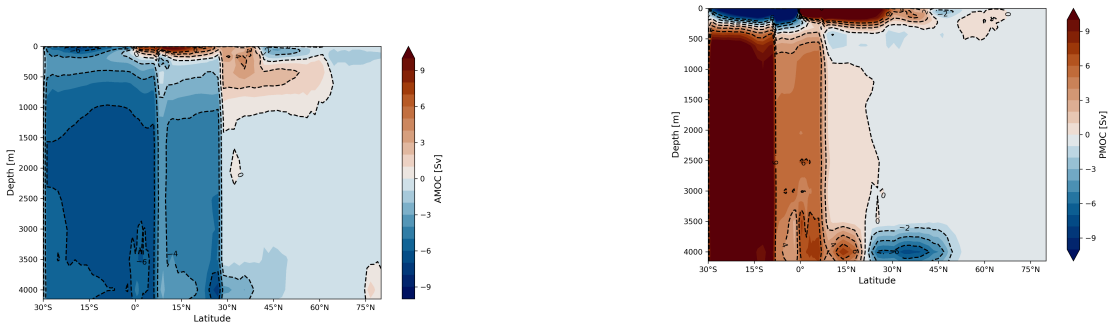

Figure 30: Antlantic meridional overturnic circulation (left) and Pacific meridional overturning circulation (right) exhibited by the fully coupled simulation CPL5-CV. The streamfunction integration is only valid above 27°N (AMOC) and 7°N (PMOC), as the integrated streamfunction shows discontinuities due to the Tethys gateway and CAS at the respective latitudes.

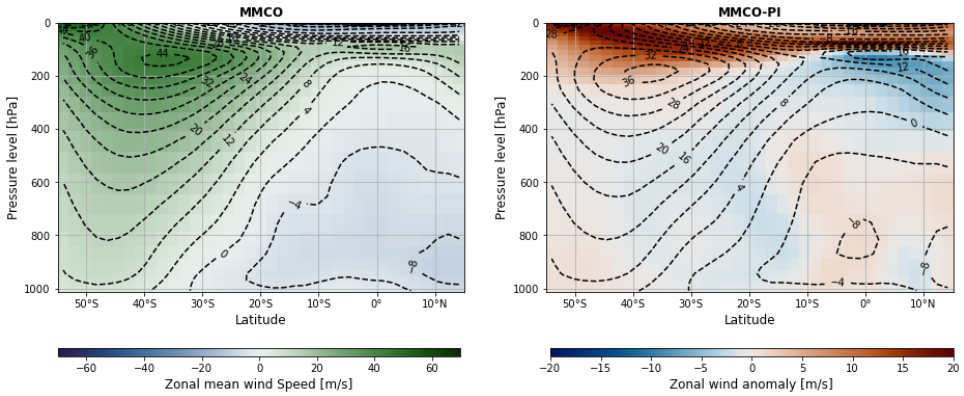

Figure 31: Zonal winds averaged over South America (80°W-35°W, analog to Figure 14. The left plot shows CPL5-CV only, the right plot shows its anomaly to the preindustrial reference simulation, with simulated PI winds shown as contours.

A.2 Supplementary Figures on LMDZOR6

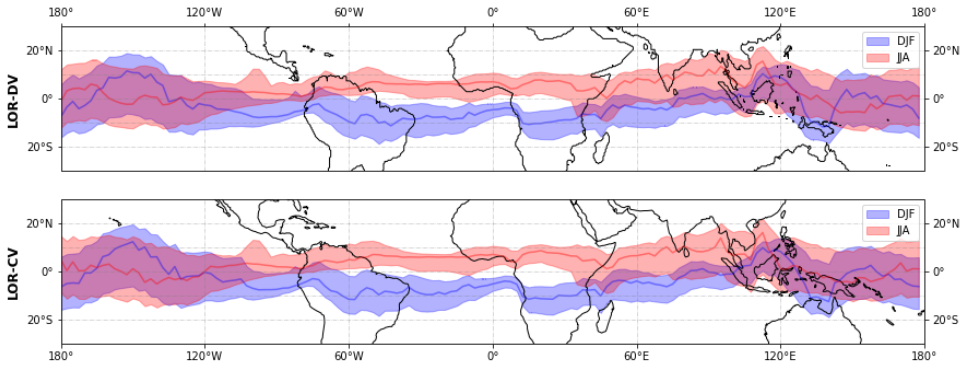

Figure 32: Seasonal ITCZ position and with simulated in LOR6-CV and LOR6-DV, analog to Figure 15.

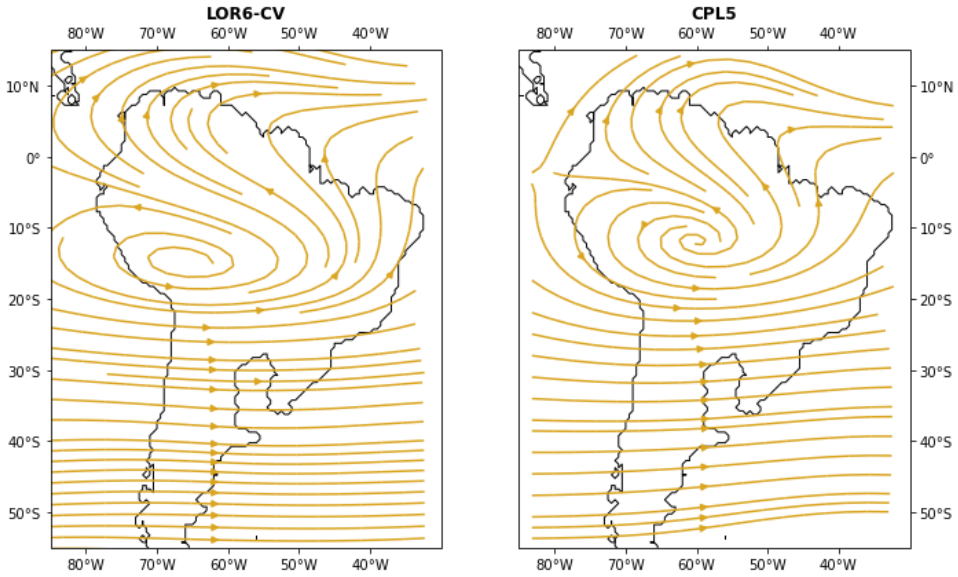

Figure 33: 200 hPa stream plot (DJF) of LOR6-DV (left) and CPL5-CV (right), for comparison of the Bolivian High.

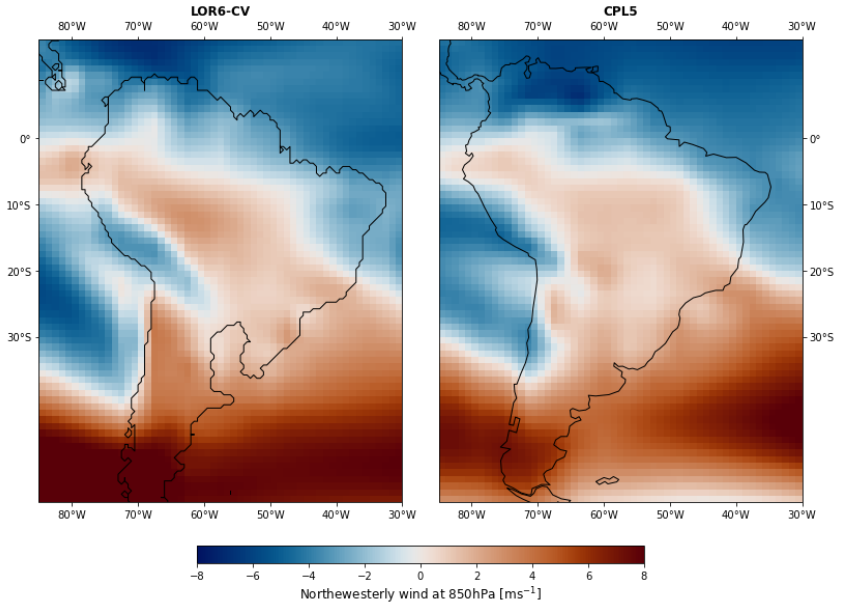

Figure 34: 850 hPa northwesterly winds during DJF for LOR6-CV and CPL5-CV for comparison of the SALLJ.

Figure 35: Regional hydrology of the simulation LOR6-CV (left) against the preindustrial IPSL-CM6-LR control simulation from CMIP6 (right)